

THE ATACAMA COSMOLOGY TELESCOPE: EXTRAGALACTIC SOURCES AT 148 GHz IN THE 2008 SURVEY

TOBIAS A. MARRIAGE^{1,31}, JEAN BAPTISTE JUIN², YEN-TING LIN^{1,2,3}, DANICA MARSDEN⁴, MICHAEL R. NOLTA⁵,
BRUCE PARTRIDGE⁶, PETER A. R. ADE⁷, PAULA AGUIRRE², MANDANA AMIRI⁸, JOHN WILLIAM APPEL⁹, L. FELIPE BARRIENTOS²,
ELIA S. BATTISTELLI^{8,10}, JOHN R. BOND⁵, BEN BROWN¹¹, BRYCE BURGER⁸, JAY CHERVENAK¹², SUDEEP DAS^{1,9,13}, MARK
J. DEVLIN⁴, SIMON R. DICKER⁴, W. BERTRAND DORIESE¹⁴, JOANNA DUNKLEY^{1,9,15}, ROLANDO DÜNNER²,
THOMAS ESSINGER-HILEMAN⁹, RYAN P. FISHER⁹, JOSEPH W. FOWLER⁹, AMIR HAJIAN^{1,5,9}, MARK HALPERN⁸,
MATTHEW HASSELFIELD⁸, CARLOS HERNÁNDEZ-MONTEAGUDO¹⁶, GENE C. HILTON¹⁴, MATT HILTON^{17,18}, ADAM D. HINCKS⁹,
RENÉE HLOZEK¹⁵, KEVIN M. HUFFENBERGER¹⁹, DAVID HANDEL HUGHES²⁰, JOHN P. HUGHES²¹, LEOPOLDO INFANTE², KENT
D. IRWIN¹⁴, MADHURI KAUL⁴, JEFF KLEIN⁴, ARTHUR KOSOWSKY¹¹, JUDY M. LAU^{9,22,23}, MICHELE LIMON^{4,9,24}, ROBERT
H. LUPTON¹, KRISTA MARTOCCI^{9,25}, PHIL MAUSKOPF⁷, FELIPE MENANTEAU²¹, KAVILAN MOODLEY^{17,18}, HARVEY MOSELEY¹²,
CALVIN B. NETTERFIELD²⁶, MICHAEL D. NIEMACK^{9,14}, LYMAN A. PAGE⁹, LUCAS PARKER⁹, HERNAN QUINTANA², BETH REID^{9,27},
NEELIMA SEHGAL²², BLAKE D. SHERWIN⁹, JON SIEVERS⁵, DAVID N. SPERGEL¹, SUZANNE T. STAGGS⁹, DANIEL S. SWETZ^{4,14},
ERIC R. SWITZER^{9,25}, ROBERT THORNTON^{4,28}, HY TRAC^{1,29}, CAROLE TUCKER⁷, RYAN WARNE¹⁷, GRANT WILSON³⁰,
ED WOLLACK¹², AND YUE ZHAO⁹

¹ Department of Astrophysical Sciences, Peyton Hall, Princeton University, Princeton, NJ 08544, USA

² Departamento de Astronomía y Astrofísica, Facultad de Física, Pontificia Universidad Católica de Chile, Casilla 306, Santiago 22, Chile

³ Institute for the Physics and Mathematics of the Universe, The University of Tokyo, Kashiwa, Chiba 277-8568, Japan

⁴ Department of Physics and Astronomy, University of Pennsylvania, 209 South 33rd Street, Philadelphia, PA 19104, USA

⁵ Canadian Institute for Theoretical Astrophysics, University of Toronto, Toronto, ON M5S 3H8, Canada

⁶ Department of Physics and Astronomy, Haverford College, Haverford, PA 19041, USA

⁷ School of Physics and Astronomy, Cardiff University, The Parade, Cardiff, Wales CF24 3AA, UK

⁸ Department of Physics and Astronomy, University of British Columbia, Vancouver, BC V6T 1Z4, Canada

⁹ Joseph Henry Laboratories of Physics, Jadwin Hall, Princeton University, Princeton, NJ 08544, USA

¹⁰ Department of Physics, University of Rome “La Sapienza,” Piazzale Aldo Moro 5, I-00185 Rome, Italy

¹¹ Department of Physics and Astronomy, University of Pittsburgh, Pittsburgh, PA 15260, USA

¹² Code 553/665, NASA/Goddard Space Flight Center, Greenbelt, MD 20771, USA

¹³ Berkeley Center for Cosmological Physics, LBL and Department of Physics, University of California, Berkeley, CA 94720, USA

¹⁴ NIST Quantum Devices Group, 325 Broadway Mailcode 817.03, Boulder, CO 80305, USA

¹⁵ Department of Astrophysics, Oxford University, Oxford OX1 3RH, UK

¹⁶ Max Planck Institut für Astrophysik, Postfach 1317, D-85741 Garching bei München, Germany

¹⁷ Astrophysics and Cosmology Research Unit, School of Mathematical Sciences, University of KwaZulu-Natal, Durban 4041, South Africa

¹⁸ Centre for High Performance Computing, CSIR Campus, 15 Lower Hope Street Rosebank, Cape Town, South Africa

¹⁹ Department of Physics, University of Miami, Coral Gables, FL 33124, USA

²⁰ Instituto Nacional de Astrofísica, Óptica y Electrónica (INAOE), Tonantzintla, Puebla, Mexico

²¹ Department of Physics and Astronomy, Rutgers, The State University of New Jersey, Piscataway, NJ 08854-8019, USA

²² Kavli Institute for Particle Astrophysics and Cosmology, Stanford University, Stanford, CA 94305-4085, USA

²³ Department of Physics, Stanford University, Stanford, CA 94305-4085, USA

²⁴ Columbia Astrophysics Laboratory, 550 West 120th Street, Mail Code 5247, New York, NY 10027, USA

²⁵ Kavli Institute for Cosmological Physics, Laboratory for Astrophysics and Space Research, 5620 South Ellis Avenue, Chicago, IL 60637, USA

²⁶ Department of Physics, University of Toronto, 60 St. George Street, Toronto, ON M5S 1A7, Canada

²⁷ ICREA & Institut de Ciències del Cosmos (ICC), University of Barcelona, Barcelona 08028, Spain

²⁸ Department of Physics, West Chester University of Pennsylvania, West Chester, PA 19383, USA

²⁹ Harvard-Smithsonian Center for Astrophysics, Harvard University, Cambridge, MA 02138, USA

³⁰ Department of Astronomy, University of Massachusetts, Amherst, MA 01003, USA

Received 2010 July 29; accepted 2011 February 18; published 2011 March 29

ABSTRACT

We report on extragalactic sources detected in a 455 deg² map of the southern sky made with data at a frequency of 148 GHz from the Atacama Cosmology Telescope (ACT) 2008 observing season. We provide a catalog of 157 sources with flux densities spanning two orders of magnitude: from 15 mJy to 1500 mJy. Comparison to other catalogs shows that 98% of the ACT detections correspond to sources detected at lower radio frequencies. Three of the sources appear to be associated with the brightest cluster galaxies of low-redshift X-ray-selected galaxy clusters. Estimates of the radio to millimeter-wave spectral indices and differential counts of the sources further bolster the hypothesis that they are nearly all radio sources, and that their emission is not dominated by re-emission from warm dust. In a bright (>50 mJy) 148 GHz selected sample with complete cross-identifications from the Australia Telescope 20 GHz survey, we observe an average steepening of the spectra between 5, 20, and 148 GHz with median spectral indices of $\alpha_{5-20} = -0.07 \pm 0.06$, $\alpha_{20-148} = -0.39 \pm 0.04$, and $\alpha_{5-148} = -0.20 \pm 0.03$. When the measured spectral indices are taken into account, the 148 GHz differential source counts are consistent with previous measurements at 30 GHz in the context of a source count model dominated by radio sources. Extrapolating with an appropriately rescaled model for the radio source counts, the Poisson contribution to the spatial power spectrum from synchrotron-dominated sources with flux density less than 20 mJy is $C^{\text{Sync}} = (2.8 \pm 0.3) \times 10^{-6} \mu\text{K}^2$.

Key words: cosmic background radiation – galaxies: active – radio continuum: galaxies – surveys

1. INTRODUCTION

Large ($>100 \text{ deg}^2$) millimeter-wave surveys are beginning to probe arcminute angular scales, corresponding to spatial frequencies $\ell > 3000$. At these small angular scales, the fluctuations in the extragalactic sky temperature become dominated by emission from galaxies and the thermal Sunyaev–Zel’dovich (SZ) effect from galaxy clusters (Sunyaev & Zel’dovich 1970), rather than primordial fluctuations in the Cosmic Microwave Background (CMB).

The predominant extragalactic point sources of emission at 148 GHz (2.0 mm) are active galactic nuclei (AGNs) and dusty, star-bursting galaxies. AGNs detected at 148 GHz are characterized by a synchrotron-dominated spectrum extending to lower radio frequencies. On the other hand, dusty, star-bursting galaxies at 148 GHz display a gray body spectrum increasing with frequency into the submillimeter. The source of 148 GHz flux from AGNs is synchrotron emission concentrated near the central accreting super massive black hole while for dusty star-bursting galaxies the millimeter flux is sourced by re-emission from dust that is heated primarily by prodigious star formation. While the millimeter emission from the majority of dusty star-bursting galaxies is below the nominal flux density limits of current large-scale surveys, a recent 150 and 220 GHz study by Vieira et al. (2010) using the South Pole Telescope (SPT) identifies a subpopulation of these sources with anomalously high fluxes which likely belong to a rare, lensed population of high-redshift dusty galaxies (Negrello et al. 2007; Lima et al. 2010). It follows that current and future wide-area millimeter surveys will identify important subpopulations of core-exposed, radio-loud AGNs and lensed dusty galaxies. With the members of these subpopulations identified, detailed follow-up studies will help us better understand these high-energy states of galaxy formation as well as their important role in providing energy feedback to their environments.

Because source emission is a significant contributor to the overall sky brightness at small scales, the characterization of extragalactic sources is essential for interpreting the primary CMB anisotropies and the SZ signal from galaxy clusters. Measurements of the primary CMB power spectrum at high spatial frequencies ($\ell \geq 2000$) will constrain the form of the inflationary potential (e.g., the spectral index n_s of primordial fluctuations). Such measurements will require information about the spectral and spatial distribution of millimeter sources in order to separate foregrounds from the primordial signal. At still smaller scales ($\ell > 3000$), studies of the CMB spectrum attempt to constrain fluctuations in the matter density field from the contribution of the SZ to the power spectrum (Lueker et al. 2010; Fowler et al. 2010). For these studies an in-depth understanding of the point source populations is even more critical for separating the power spectrum of the SZ from that of sources. Furthermore, an understanding of the energy feedback from AGN and star formation to the cluster environment will be important for constraining the form of the SZ spectrum (Battaglia et al. 2010; Shaw et al. 2010; Trac et al. 2011). Finally, SZ surveys attempting to measure Ω_M , σ_8 , and dark energy through the evolution of the cluster mass function will likewise need to consider the spectral behavior and cluster occupation numbers for sources in order to avoid systematically biasing mass estimates based on the SZ flux density (Lin et al. 2009; Sehgal et al. 2010; Vanderlinde et al. 2010).

The Atacama Cosmology Telescope (ACT) is a millimeter-wave observatory which will ultimately survey thousands of square degrees of sky at arcminute resolution with milli-Jansky sensitivity to sources. ACT is located at 5200 m in the Atacama Desert in the Andes of northern Chile.³² This high desert site in the tropics was chosen for its excellent atmospheric transparency and its access to northern and southern celestial latitudes. ACT observes simultaneously in bands centered at 148 GHz (2.0 mm), 218 GHz (1.4 mm), and 277 GHz (1.1 mm), each band having a dedicated 1024-element array of bolometric transition edge sensors. As of mid-2010, ACT has completed three seasons of observations: 2007, 2008, and 2009, and the 2010 season is underway. In each season, ACT has conducted two surveys: a 9° -wide survey centered at decl. $-53^\circ 5'$ and a 5° -wide stripe centered on the celestial equator.

In this paper, we report on extragalactic sources in the ACT 2008 148 GHz data set. This is the first report devoted to ACT source science and complements the 148 GHz power spectrum study in Fowler et al. (2010). In what follows, we give an overview of the observations and data reduction (Section 2), describe the source catalog (Section 3 and the Appendix), and discuss implications of the study including constraints on source models (Section 4).

2. OBSERVATIONS AND DATA REDUCTION

The data used for this analysis were collected by ACT at 148 GHz during its second observing season in 2008. This section gives an overview of the survey observations and the reduction of the raw data to a map as well as a detailed description of the source extraction. For a more thorough introduction to the ACT facility, observations, and data reduction pipeline, we refer the reader to Fowler et al. (2010), Swetz et al. (2010), and references therein.³³

2.1. Observations

The 2008 southern observations were carried out over a survey area 9° wide, centered on decl. $-53^\circ 5'$, and extending from R.A. 19^{h} to 24^{h} and 00^{h} to $07^{\text{h}}30^{\text{m}}$. The subset of these data used in the present analysis lies between R.A. $00^{\text{h}}12^{\text{m}}$ and $07^{\text{h}}08^{\text{m}}$ and decl. $-56^\circ 11'$ and $-49^\circ 00'$ (455 deg^2). The area was chosen to encompass the data used for power spectrum work in Fowler et al. (2010) and represents a large fraction of the most deeply covered regions from the 2008 148 GHz data set. Figure 1 shows the area of the sky used and associated point source sensitivities. Typical white noise levels in the map are $30\text{--}50 \mu\text{K}$ arcmin, tending to higher values toward the map boundaries. As described in Section 2.4, this white noise level, when match filtered with the ACT beam, results in typical sensitivities to point source flux densities from 2.5 to 5 mJy.

The 2008 ACT observing season extended from mid-August to the final week of December. Observations took place during nighttime hours: from roughly 20:00 to 06:00 local time. Of the total observing time, approximately 85% was devoted to the southern region. ACT observed by scanning at a constant elevation of $50^\circ 5'$ while the survey region drifted through the scan with the rotation of the Earth. During the first half of a night, ACT scanned at azimuth 150° , targeting a rising section of the survey area. During the second half of the night, ACT scanned the same section setting on the other side of the south

³¹ Current address: Department of Physics and Astronomy, The Johns Hopkins University, 3400 North Charles Street, Baltimore, MD 21218-2686, USA.

³² The ACT Site is at $22^\circ 9' 58.6''$ south latitude, $67^\circ 7' 8.75''$ west longitude.

³³ ACT Collaboration papers are archived at <http://www.physics.princeton.edu/act/>.

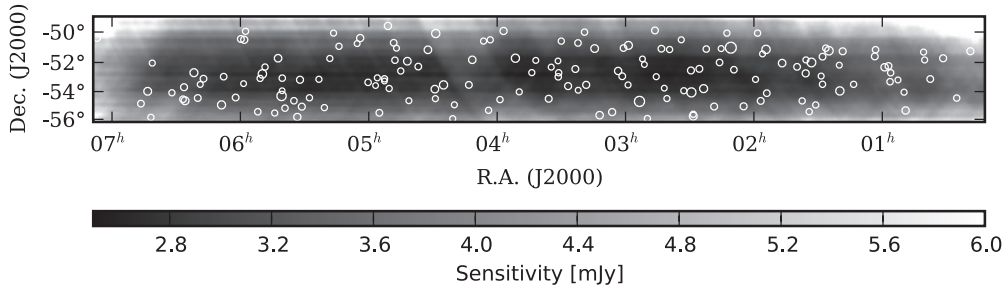


Figure 1. Sensitivity map with detections. The subset of the ACT 2008 148 GHz data set considered for this study lies between R.A. $00^{\text{h}}12^{\text{m}}$ and $07^{\text{h}}08^{\text{m}}$ and decl. $-56^{\circ}11'$ and $-49^{\circ}00'$ (455 deg^2). The grayscale encodes the rms of the map in mJy. The deepest data correspond to an exposure time of 23.5 minutes per square arcmin and a 1σ sensitivity of 2.5 mJy. White circles mark the locations of ACT sources. The diameter of each circle is proportional to the log of the associated source flux density. Toward the edge of the map, the noise properties display local variation. For this reason, detections with flux density values below 50 mJy have been discarded in regions where the rms exceeds 4.6 mJy, corresponding to less than 7 minutes of integration. This, together with an exclusion of all detections below 5.25σ , accounts for the relative dearth of detections in areas of shallow coverage (see Section 2.4).

celestial pole at azimuth 210° . The rising scans cross the survey region from southwest to northeast and back (in equatorial coordinates), while the setting scans cross the survey region from southeast to northwest. Together, the rising and setting scans cross link each point on the sky with all adjacent points. The resulting cross-linked temperature data in principle contain all information necessary to recover an unbiased, low-noise map of the millimeter sky. In addition to survey observations, ACT also executed regular observations of Uranus and Saturn during 2008 to provide gain calibration, beam profiles, and pointing.

With the telescope scan strategy described above, any given location in the survey area would be observed over a period of approximately two months during a season. Therefore, source flux densities reported here are the average flux density over a two-month period. This is an important point as the vast majority of sources presented in this paper are AGNs which are known to be variable (e.g., Kesteven et al. 1977; Valtaoja et al. 1992).

2.2. Reduction to Maps

The raw 148 GHz data consist of 1024 time-ordered data streams, one per element of the detector array. Approximately 25% of the data are rejected on the basis of telescope operation and weather. After further cuts based on individual detector performance, the data from 680 148 GHz detectors over 850 hr ($\sim 3200 \text{ GB}$) are retained from the 2008 southern survey.

Pointing reconstruction is accomplished in two steps. First, the relative detector pointings are established with $1''.2$ certainty through observations of Saturn. Second, absolute detector array pointings for our two southern survey configurations (rising and setting; 150° and 210° azimuth, 50.5° elevation) are established with $3''.5$ precision through an iterative process in which the absolute pointing is adjusted based on offsets of ACT-observed radio source locations with respect to source locations taken from the Australia Telescope 20 GHz (AT20G) survey (Murphy et al. 2010).

Nightly calibrations of the detectors' responsivity (power-to-current conversion) are based on load curves taken at the start of each night. Stability of this calibration through the night is monitored using small steps in the detector bias voltages and established at the few percent level. Relative detector flux density calibrations are based on normalizing the detector responses to the beam-filling atmospheric signal. The resulting relative calibration is shown to be constant through the season at the few percent level. The final brightness temperature calibration is based on ACT observations of Uranus throughout the season and the WMAP7 Uranus temperature (Weiland

et al. 2011) extrapolated to the ACT 148 GHz band. The calibration is more fully described in Fowler et al. (2010). The overall calibration is certain to 6% rms, a number dominated by systematic uncertainties in extrapolating the temperature of Uranus to 148 GHz from *Wilkinson Microwave Anisotropy Probe* (WMAP) frequencies.

The final step in the data reduction is map-making. An iterative preconditioned conjugate gradient solver is used to recover the maximum likelihood (ML) maps. The algorithm solves simultaneously for the millimeter sky as well as correlated noise (e.g., a common mode from atmospheric emission). The map projection used is cylindrical equal area with a standard latitude of -53.5 and 0.5 square pixels. For more details on the mapping and other reduction steps, refer to Fowler et al. (2010).

2.3. Data Modeling

The next step toward a source catalog is the construction of a filter which optimizes the signal-to-noise ratio (S/N) of sources in the 148 GHz map.³⁴ In order to construct such a filter, it is necessary to obtain best estimates of the power spectra of the different components, signal and noise, which contribute to the ACT data. We model the temperature T at position \mathbf{x} as the sum over sources plus other components in the map:

$$T(\mathbf{x}) = \sum_i T_i b(\mathbf{x} - \mathbf{x}_i) + T_{\text{other}}(\mathbf{x}), \quad (1)$$

where T_i is the peak amplitude of the i th source, b is the ACT 148 GHz beam function normalized to unit amplitude and taken to be isotropic (Hincks et al. 2010), and T_{other} includes contributions from the primary CMB, undetected point sources, SZ from clusters, and noise from the detectors and atmosphere.

Figure 2 shows graphs of the power spectra of the contributors to T_{other} . For the primary CMB component, we use the WMAP5 best-fit model from Nolte et al. (2009). The SZ and undetected source components are taken from models fit to the ACT 148 GHz power spectrum in Fowler et al. (2010). The spatial power spectrum from Fowler et al. (2010) was computed after masking sources from a preliminary version of the catalog presented in this paper. As such the derived contribution to T_{other} from undetected sources should be a suitable estimate for the matched filter in this work. Specifically, the source model is a Poisson spectrum normalized to $\ell(\ell+1)C_p/2\pi = 11.2 \mu\text{K}^2$ at $\ell = 3000$, and the SZ model is a combined thermal and kinetic

³⁴ See Section 2.4 for the definition of S/N used in this work.

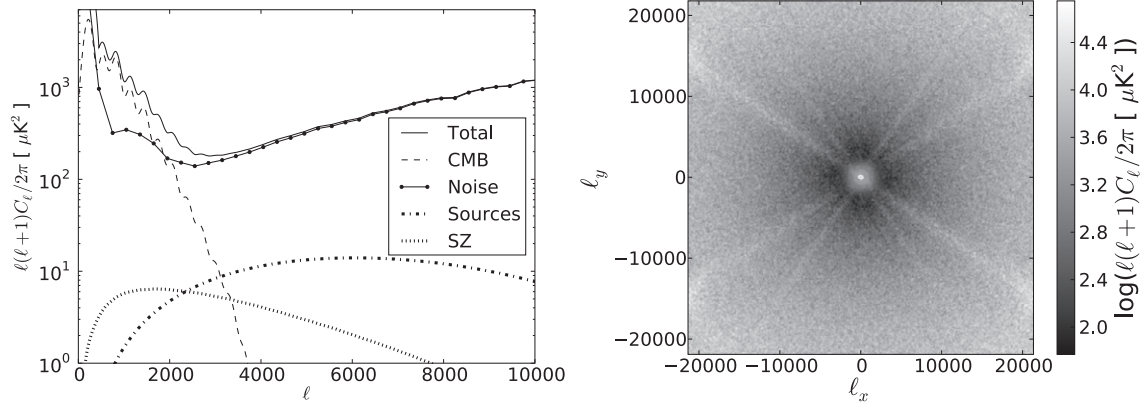


Figure 2. Model ACT auto-power spectra used for the matched filter. Left: one-dimensional spectra decomposed by component. The CMB spectrum is taken from WMAP5 (Nolta et al. 2009). The undetected sources and the SZ effect from galaxy clusters are one-dimensional templates fit to the high- ℓ 148 GHz spectrum in Fowler et al. (2010). The one-dimensional noise spectrum is obtained by radially binning the average of two-dimensional spectra from ACT 148 GHz jackknife maps. The spectra are dominated at low ℓ by the CMB and atmospheric noise and at high ℓ by white detector and photon shot noise. Convolution of all celestial components by the ACT beam results in attenuation of the corresponding spectra at high ℓ . Right: the model two-dimensional auto power spectrum. The spectrum includes noise, CMB, undetected sources, and the SZ effect from galaxy clusters. The latter three components were obtained from the one-dimensional models. The ACT noise is isotropic except for extra noise in scan parallel (from residual $1/f$) and scan perpendicular (from detector row correlations) directions. For each rising and setting scan direction, two orthogonal bands of excess power are centered on the origin rotated 60° with respect to one another. To minimize contamination, it is important to deweight data in these diagonal modes through the two-dimensional matched filter.

SZ model ($\sigma_8 = 0.8$) from Sehgal et al. (2010) normalized by a best-fit factor of 0.63. These celestial models (CMB, sources, and SZ) are all convolved with the ACT 148 GHz beam function. The celestial models are natively one-dimensional functions of multipole ℓ (as shown in the left graph of Figure 2) with corresponding azimuthally symmetric two-dimensional representations (as shown in the right graph of Figure 2). The noise term, on the other hand, is natively a two-dimensional power spectrum estimated by the average of power spectra from difference maps. The difference maps were constructed by subtracting a map made from one half of the data (with a random selection of observing days contributing) from a map made from the other half (using the remaining observing days). The two-dimensional noise power spectrum is binned radially to obtain the one-dimensional representation shown by the line of connected dots in the left graph of Figure 2.

From Figure 2, it is clear that the primary contributions to T_{other} come from the CMB and atmosphere at large scales ($\ell < 2500$), while the white detector and photon shot noise dominates the power at small scales. In the spectral trough around $\ell = 2500\text{--}3500$, the detectable sources will have their greatest S/N.

An important feature of the two-dimensional power spectrum in the right graph of Figure 2 is the anisotropic nature of the noise term which corresponds to striping in the map. The stripes are a result of large-scale drifts in atmospheric emission along the scan directions as well as from correlations among rows of ACT detectors perpendicular to the scan directions. Accounting for this anisotropy when filtering the map is important for extracting an uncontaminated sample of sources. To properly downweight these noisy diagonal modes, we adopt a two-dimensional noise covariance in the matched filtering technique described in Section 2.4.

The final significant noise term that is not captured in difference maps is consistent with scan synchronous noise. The noise is likely due to instabilities induced by acceleration at scan turnarounds. The noise manifests itself as horizontal striping in the maps and as excess power isolated to a vertical strip $-100 < \ell_x < 100$ in Fourier space. For simplicity, we set the noise power to infinity in this section of Fourier space

such that modes contaminated by this noise will be completely downweighted by the filter as described in the following section.

2.4. Detection and Catalog Construction

To optimize the S/N of the sources with respect to the background, we use a matched filter. This approach has been proposed and used in previous work to find both sources (Tegmark & de Oliveira-Costa 1998; Wright et al. 2009; Vieira et al. 2010) and the SZ effect from clusters (Melin et al. 2006; Staniszewski et al. 2009). For completeness of presentation, here we rederive the form of the filter and its basic properties. Without loss of generality, we consider a field centered on a source such that

$$T(\mathbf{x}) = T_0 b(\mathbf{x}) + T_{\text{other}}(\mathbf{x}). \quad (2)$$

We apply a filter $\Phi(\mathbf{k})$ in Fourier space such that the temperature at the center of filtered field is

$$T_{\text{filt}}(0) = T_0 \int \Phi(\mathbf{k}) \tilde{b}(\mathbf{k}) d\mathbf{k} + \int \Phi(\mathbf{k}) \tilde{T}_{\text{other}}(\mathbf{k}) d\mathbf{k}, \quad (3)$$

where \tilde{b} and \tilde{T}_{other} are the Fourier transform of the beam and noise temperature field, respectively. The S/N of the central source is

$$\text{S/N} = \frac{|T_0 \int \Phi(\mathbf{k}) \tilde{b}(\mathbf{k}) d\mathbf{k}|}{|\int \Phi(\mathbf{k}) \tilde{T}_{\text{other}}(\mathbf{k}) d\mathbf{k}|}. \quad (4)$$

A filter that maximizes this S/N is

$$\Phi(\mathbf{k}) = \frac{\tilde{b}^*(\mathbf{k}) |\tilde{T}_{\text{other}}(\mathbf{k})|^{-2}}{\int \tilde{b}^*(\mathbf{k}') |\tilde{T}_{\text{other}}(\mathbf{k}')|^{-2} \tilde{b}(\mathbf{k}') d\mathbf{k}'}, \quad (5)$$

where the normalization has been chosen to produce an unbiased estimate of the amplitude of the source T_0 at $\mathbf{x} = 0$. The noise variance of the filtered data is

$$\begin{aligned} \sigma^2 &= \int |\Phi(\mathbf{k}) \tilde{T}_{\text{other}}(\mathbf{k})|^2 d\mathbf{k} \\ &= \left[\int \tilde{b}^*(\mathbf{k}) |\tilde{T}_{\text{other}}(\mathbf{k})|^{-2} \tilde{b}(\mathbf{k}) d\mathbf{k} \right]^{-1}. \end{aligned} \quad (6)$$

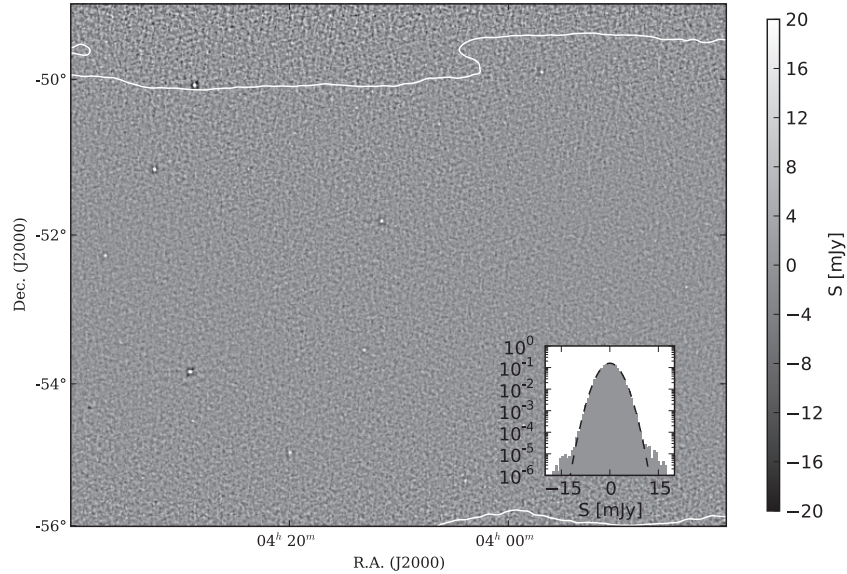


Figure 3. 148 GHz map. The submap shown above is a sample 64 deg^2 of the survey field. The data have been match filtered such that the grayscale is in units of flux density (mJy). The inset shows the flux density distribution across the data weighted by the max-normalized square root of the number of data per pixel $\sqrt{N_{\text{obs}}(\mathbf{x})}/\sqrt{N_{\text{obs,max}}}$. Thus, the distribution represents the data in the deepest part of the map (although it uses weighted data from all regions). The data distribution is shown as a gray histogram on which is plotted a dashed Gaussian distribution with standard deviation 2.5 mJy. The positive non-Gaussian tail may, in part, be attributed to sources and the negative tail to ringing from the filter about sources as well as SZ (e.g., ACT-CL J0438–5419 from Menanteau et al. 2010). Several sources are apparent as white points surrounded by darker rings from the filter. The white contour marks the transition at the edge of the map where the rms exceeds 4.6 mJy, corresponding to less than 7 minutes of integration per arcminute. In this region, we have excluded detections below 50 mJy due to contamination from local noise. The source above the contour at $\delta \approx -50^\circ$ has a flux density of 150 mJy and is included in the catalog.

In practice, the noise variance of the filtered map is obtained from the filtered map itself after masking the brightest six sources ($S/N > 50$). These sources increase the rms of the maps by 10%. The remaining sources contribute approximately 1% to the rms. This slightly more conservative estimate of the variance agrees with the estimate from Equation (6) in which T_{other} has been constructed as described in Section 2.3. In what follows, the S/N at a location in the filtered map is defined as the temperature at that location divided by the square root of this variance.

Before applying the global matched filter from Equation (5), we multiply the map, pixel wise, by the square root of the number of observations per pixel normalized by the observations per pixel in the deepest part of the map, $\sqrt{N_{\text{obs}}(\mathbf{x})/N_{\text{obs,max}}}$. This is equivalent to weighting the data by the inverse of the estimated white noise rms shown in Figure 1 and accounts for local variation in the white noise amplitude. Furthermore, the map is tapered to zero in a $10'$ boundary region around the edge of the map to mitigate the artifacts arising from data aperiodicity when filtering. These windowed data are excluded from the final analysis, reducing the usable sky area from the total 455 deg^2 to 443 deg^2 . Next, because the ringing of the filter around the brightest sources can cause false detections, we identify and mask the six most significant ($>50\sigma$) sources before applying the matched filter to the map. These brightest sources are treated and included in the catalog in the same manner as the fainter sources with the exception they are recovered through an initial run of the pipeline with the S/N lower limit increased. An important final caveat: in constructing the noise term \tilde{T}_{other} , the component models need to be tapered and weighted in the same fashion as the data for the matched filter formalism to hold. This is particularly true for components with red spatial spectra, such as the atmosphere and CMB, because aliasing due to a particular windowing scheme can significantly alter the spectrum. Figure 3

shows a sample 64 deg^2 of the filtered map. For this reason, the catalog includes only detections with S/N 5.25 and above. See Section 3.3 for a discussion of purity determination.

Localized, non-white noise in the map requires that we take further measures beyond the global matched filter solution outlined above. First, local large-scale atmospheric noise requires us to add a low- ℓ taper to the term $|T_{\text{other}}(\mathbf{k})|^{-2}$ (Equation (5)) which rises from zero at $\ell = 0$ to one at $\ell = 1200$ as $\sin^5(\pi\ell/2400)$. This filter removes the local atmospheric noise while downweighting only a small fraction ($\sim 1\%$) of the data containing source power in Fourier space. Second, in areas of the map which are particularly shallow, uneven coverage leads to excess striping. In these parts of the map, the noise model described in Section 2.3 is invalid and non-white noise remains even after the filter is applied. For this reason, we exclude sources from the catalog which are detected with flux densities below 50 mJy in areas of the map with exposure times less than 7 minutes per square arcminute. This exposure time is approximately one-third the exposure time in the deepest areas of the map and corresponds to 4.6 mJy rms. The cut level of 50 mJy at 7 minutes per square arcminute was chosen to broadly eliminate contamination observed in simulations. Future studies will make use of local noise estimation to avoid such an exclusion. The sample submap in Figure 3 demarcates the region at the edge of the map in which we exclude 50 mJy detections with a white contour. With this exclusion, the area used for sources with flux density below 50 mJy is 366 deg^2 .

The final step in the catalog generation is to derive the flux densities associated with the detections. Given the form of the filter in Equation (5), the source-centered value of the filtered map, multiplied by the solid angle of the beam profile, is the source flux density. It is this value, rescaled by the inverse of the square root of the number of observations per pixel normalized by the number of observations per pixel in the deepest part of the

map ($\sqrt{N_{\max}/N_{\text{obs,max}}(\mathbf{x})}$), that we record as the raw flux density estimate for a detection. It follows that an error in source location results in an error in flux estimation. Such an error arises due to finite pixel size: a detection rarely falls in the center of a pixel. Source location error due to finite pixel size causes a systematic negative bias and increased scatter. The 0.5 ACT map pixels cause a 10% negative bias with comparable scatter in the flux density estimate. To remove this bias and scatter, we zero-pad the filtered data in Fourier space (e.g., Press et al. 1992) such that the pixel spacing in map space is decreased by a factor of 16. This Fourier interpolation of the filtered data onto 0.03125 pixels is a convenient way to better locate the peak of source emission and therefore mitigate systematic errors in position and flux density estimation to less than 1%. An important caveat to this technique is that the pixel window function must be taken into account when reducing the pixel size. As discussed further in Section 3.2.3, simulations show that flux densities thus derived are unbiased at the subpercent level.

3. CATALOG

The catalog of 157 ACT extragalactic sources is given in Table A1 of the Appendix. The catalog provides the IAU name, celestial coordinates (J2000) as well as S/N and 148 GHz flux density estimation of each ACT-detected source. Raw flux densities are estimated directly from the map as described in Section 2.4. Deboosted flux densities (Section 3.2.2) are also given. The seventh column gives the exposure time in minutes per square arcminute at the location of the source. Finally, we provide the ID of AT20G sources collocated within 30" of an ACT source. The following subsections provide the necessary information for interpreting the catalog data.

3.1. Astrometric Accuracy

The positions of the 27 ACT sources with S/N > 20 were compared to positions of associated sources in the AT20G catalog. The AT20G pointing is checked against Very Long Baseline Interferometry measurements of International Celestial Reference Frame calibrators and is shown to be accurate to better than 1 arcsecond (Murphy et al. 2010). Figure 4 shows the offsets of the 27 ACT source locations with respect to associated AT20G locations. The mean of the offsets is $-0'.3 \pm 0'.7$ in R.A. and $0'.0 \pm 0'.6$ in decl. The rms of offsets is 3'.5 in R.A. and 3'.3 in decl. One ACT source with S/N > 20 is cross-identified with an AT20G source 18" away. This source is ACT-S J042906–534943 and is flagged as extended in the AT20G catalog. Furthermore, there are multiple Sydney University Molonglo Sky Survey (SUMSS) sources located within the search radius suggesting a non-trivial geometry. Therefore, this source represents an outlier in this analysis and is not used. For 24 cross-identified sources with S/N < 8, the ACT location rms with respect to AT20G position was inflated by the effect of the noise: 8'.8 in R.A. and 6'.2 in decl.

We have identified a systematic shift in pointing throughout the season likely associated with movement of the telescope. A significant fraction of the scatter in Figure 4 is attributable to this systematic effect. Because of this effect, the distribution of pointing errors in Figure 4 does not appear Gaussian. We plan to eliminate this effect in a future study.

3.2. Flux Density Recovery

As discussed in Section 2.2, the overall calibration has an uncertainty of 6%, dominated by systematic errors in the

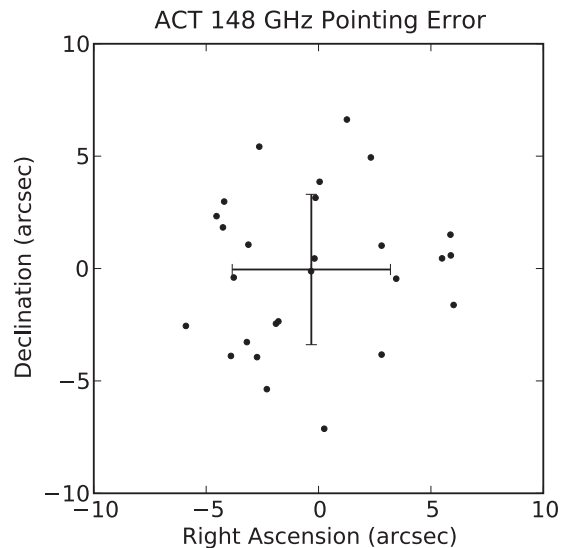


Figure 4. Astrometric accuracy. The small filled circles are the positional offsets of ACT sources with S/N > 20 from counterparts in AT20G. The error bars show the rms in R.A. (3'.5) and decl. (3'.3) and are centered on the mean of the distribution: $-0'.3 \pm 0'.7$ in R.A. and $0'.0 \pm 0'.6$ in decl.

temperature of Uranus. In addition to this uncertainty, errors in the flux estimation may arise due to errors in the assumed source profile, flux boosting of lower significance candidates, and a failure of the map maker to converge. In this section, we describe tests of these potential sources of flux density error as well as an end-to-end check of the match-filter recovery and deboosting through simulations.

3.2.1. Beam Profile

Flux density recovery is a function of the form of the source profile b assumed in the filter (see Equations (2) and (5)). For the filter's source profile b , we adopt the ACT 148 GHz beam from Hincks et al. (2010). Deviation of the actual source profile from the ACT 148 GHz beam will result in a biased estimate of the flux density as determined from the filtered map.

To search for a difference between the actual and assumed profiles, we examine the profiles of the 20 most significant sources in the ACT map. We fit the data with a background term plus an altered ACT beam (respectively, broadened or squeezed by the convolution or deconvolution with a Gaussian). The Gaussian convolution we employed models the broadening of the beam resulting from the random pointing error. The average best-fitted profile is the beam from Hincks et al. (2010) convolved with a Gaussian with $\sigma = +3'' \pm 1''$. This smearing is consistent with the pointing rms in Figure 4. The fit is performed out to a radius of 3'. Figure 5 shows the fit for the brightest source. The effect of this convolution on the 84" FWHM of the ACT beam is at the subpercent level: 0'.05. Flux density misestimation will scale roughly as the ratio of the actual profile solid angle to the assumed profile solid angle. In the present case, the misestimation is below 1%.

As an additional check on the reported flux densities, the matched filter-based flux density estimates are compared to 1' diameter aperture flux densities. The aperture flux density is defined as the background-subtracted flux within a circle (the aperture) centered on the source. The aperture flux density is estimated from the unfiltered ACT maps and as such is complementary to the flux density estimates from the filtered maps. As the source profile extends well beyond a 1' diameter,

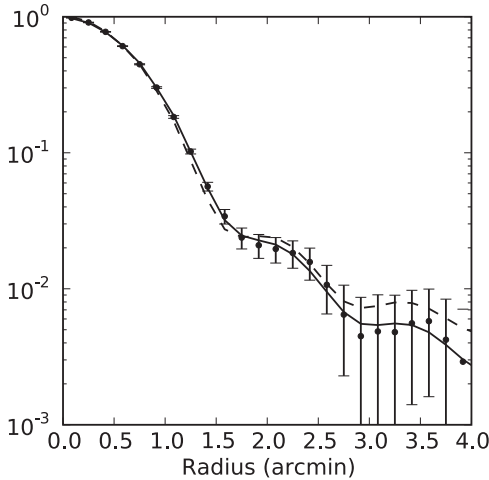


Figure 5. Source profile fitting. The radially binned and normalized brightness profile observed for ACT-S J021046–510100 is represented by the points with error bars. The solid line running through the points is the measured ACT beam from Hincks et al. (2010) convolved with a Gaussian with $\sigma = 3''$ plus an additive background term. The Gaussian convolution is intended to represent spreading of the beam by random pointing error. The value of $\sigma = 3''$ describes the best fit to a Gaussian-convolved beam plus background term. Note that $3''$ is consistent with pointing uncertainty from Figure 4. The dashed line shows the model with background and beam amplitude fit to the data, but no Gaussian convolution. Without the Gaussian convolution, the background term increases to fit the data at small angles and forces the model high at large angles. The data clearly prefer the Gaussian-convolved model. Similar fits to the 20 brightest sources in the ACT data suggest bias in the reported flux density level due to misestimation of the source profile is at the subpercent level. The error bars shown on the radially binned points are correlated.

the aperture flux density estimates are expected to be biased low with respect to true flux density. For the 30 brightest sources from the ACT data, the average ratio of aperture flux density to matched filter flux density is 0.610 ± 0.003 . In simulations which featured sources with the ACT beam shape, the same ratio is 0.607 ± 0.004 . If the source profiles in the data were different from the ACT beam shape, then this ratio from the simulation would differ from the data. The agreement between data and simulation further bolsters the claim that flux density bias due to source profile misestimation is at the subpercent level.

3.2.2. Deboosting

In a source population for which the counts are a steeply falling function of flux, a source’s measured flux density S_m in the presence of noise is likely to be an overestimate of its intrinsic value S_0 . The overestimation is most pronounced for sources at low S/N. The process of deboosting accounts for this overestimate by constructing the posterior flux distribution based on prior knowledge of the source population. Given the relatively high-flux density and significance of the detections in this work, we adopt the straightforward Bayesian approach from Coppin et al. (2005):

$$P(S_0|S_m) \propto P(S_m | S_0)P(S_0), \quad (7)$$

where the probability $P(S_m | S_0)$ of measuring S_m given S_0 is taken to be normal with mean S_0 and variance derived from the S/N.

The prior probability of flux S_0 in a pixel, $P(S_0)$, is computed by generating simulations of the (filtered) intrinsic source flux distribution per pixel. Individual, filtered source profiles, $T_0 \int \Phi(\mathbf{k})\tilde{b}(\mathbf{k})d\mathbf{k}$, are added to a blank survey map at randomly chosen locations. The numbers and associated amplitudes, T_0 ,

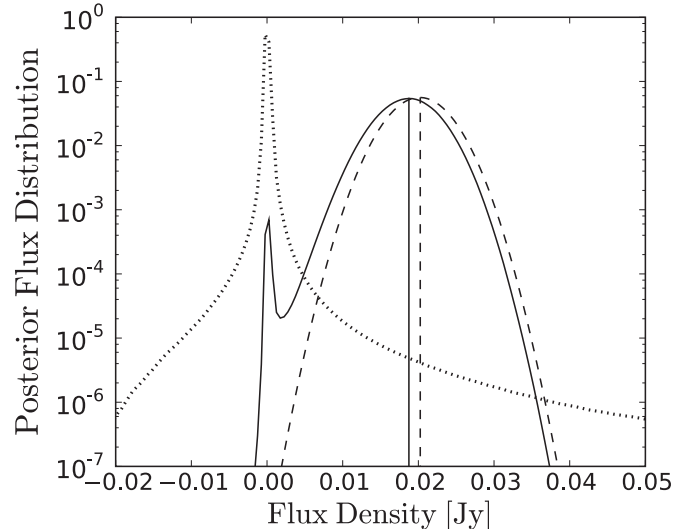


Figure 6. Flux density deboosting. The Gaussian flux density distribution $P(S_m | S_0)$ (dashed) derived directly from the maps is multiplied by the prior distribution $P(S_0)$ (dotted) of the intrinsic source flux to obtain the deboosted posterior flux distribution (solid). Since the mean of the maps is set to zero through filtering, $P(S_0)$ can assume negative values. The peak in the distribution shifts to lower density flux (a $< 10\%$ effect for 20 mJy sources). For the S/N = 5.6 source shown here, there is little volume in the posterior $P(S_m | S_0)$ at negative flux.

of the sources are chosen in accordance with infrared and radio counts from Toffolatti et al. (1998) rescaled to fit the counts from this study (see Section 4.4). The procedure for computing the prior probability based on source counts fit to our data involved an initial rescaling of the Toffolatti et al. (1998) data model to counts computed with raw flux densities. Given deboosted flux densities based on this initial prior, counts were then re-computed, the prior was re-estimated and used to obtain new deboosted flux densities. This process was iterated until corrections to the counts and the deboosted flux densities became negligible. Only one iteration was required for the relatively small level of deboosting used in this initial study. Furthermore, we cut off the radio counts at 150 mJy, reflecting the fact that the brightest six sources ($S > 150$ mJy) are detected and subtracted before constructing the rest of the catalog. A function $P_i(S_0)$ is then generated by binning the fluxes associated with map (indexed here by i) pixels in 0.5 mJy bins. The final distribution $P(S_0)$ was then computed as the average of $P_i(S_0)$ from 10,000 independent simulations. The deboosting algorithm is illustrated for a single source in Figure 6 where the dashed Gaussian represents $P(S_m | S_0)$ and the dotted profile peaking just below zero flux is the prior probability $P(S_0)$. The posterior probability $P(S_0|S_m)$ is the solid line.

The deboosted flux S_{db} reported in the ACT catalog for sources below 50 mJy is the median of the associated $P(S_0|S_m)$, and the reported asymmetric errors enclose the 68% confidence interval. The abrupt 150 mJy cutoff imposed on the radio counts in combination with finite pixel size effects the smoothness of the prior estimate $P(S_0)$ at higher fluxes. To mitigate this effect, the simulated maps used to construct the prior feature a pixel size of half that of the data (0.25). Furthermore, deboosted fluxes are only provided for sources with flux below 50 mJy where the computed prior is smooth: for sources above 50 mJy, we simply report the center and 68% confidence level of $P(S_m|S_0)$.

The prior probability $P(S_0)$ in Figure 6 is broader and, for the range of flux densities plotted, more symmetric than analogous distributions derived in previous work (e.g., Figure 6

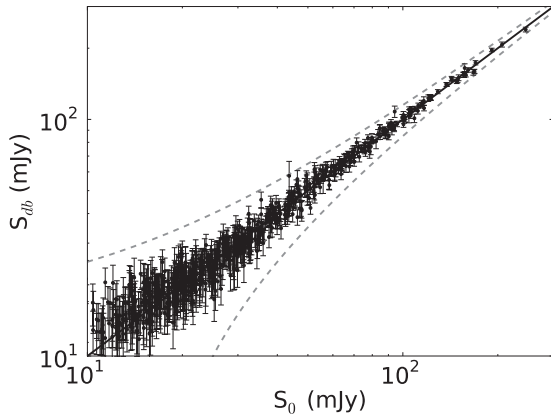


Figure 7. Simulation flux recovery. The match-filter derived and deboosted flux density estimate S_{db} plotted vs. the intrinsic flux density. The dashed gray lines show the ± 15 mJy limits about the solid black one-to-one line. For $S_0 < 20$ mJy, the sample is incomplete due to the $S/N > 5.25$ selection. This is manifest in the graph by the apparent skew of the population above the one-to-one line for low-flux densities.

of Scott et al. 2008). The difference arises because our simulations include the radio population whose source counts are much shallower than the infrared populations. The bright radio sources, in addition to having a bright positive tail, produce significant negative ringing when filtered. A more familiar form of $P(S_0)$ would be generated if we were to recover fluxes using the CLEAN technique (Högbom 1974) as described in, e.g., Vieira et al. (2010).

In future multi-band work that considers detections of lower significance, we will employ important extensions of the simple deboosting used here (e.g., Austermann et al. 2010; Crawford et al. 2010).

3.2.3. Simulations and Flux Recovery

Having established that the source profile used in the matched filter is a good approximation to that in the data (Section 3.2.1), it remains to test the flux estimation and deboosting through simulation. Source flux densities were derived from maps with celestial components and noise modeled as described in Section 2.3 with two exceptions. First, the SZ component was excluded to prevent confusion due to cluster–galaxy correlations. This effect caused negative outliers in derived flux density due to brightness cancellation by the cluster decrement. Second, we excluded several (> 10) peculiar instances of superposed, very bright, (30 mJy) infrared sources. This apparent clustering of ultra-bright dusty sources caused positive outliers in derived flux density.

With the exceptions noted above, the simulated sources were detected with the same blind algorithm that was described for source extraction from the data. Similarly, the deboosted flux densities of the simulated sources were derived. Figure 7 shows the result. At the percent level, the derived deboosted flux density S_{db} is a consistent estimate of the intrinsic flux density S_0 with a best fit of

$$S_{db} = -0.09 \pm 0.29 \text{ mJy} + 1.008 \pm 0.005 \times S_0, \quad (8)$$

where the fit (reduced $\chi^2 = 1.06$ for 451 degrees of freedom) was performed only for sources with flux density greater than 20 mJy to restrict the analysis to a complete (and thus symmetric) distribution. The errors (68% c.l.) are derived from 1000 bootstrap samplings. Furthermore, the model $S_{db} = S_0$ fits

the 451 sources with flux densities greater than 20 mJy with a reduced $\chi^2 = 1.07$. This one-to-one model fits the entire population (down to the $S/N = 5.25$) with reduced $\chi^2 = 1.19$ over 651 degrees of freedom. This improbable statistic likely results from a combination of unaccounted-for astrophysics (e.g., source clustering) in Sehgal et al. (2010), errors in our deboosting, and an underestimate of flux density error.

3.2.4. Convergence

As described in Section 2, ML maps generated from the cross-linked ACT 148 GHz data are unbiased for modes corresponding to multipoles in excess of a few hundred (i.e., exactly those used for source flux estimation). We checked this claim through signal-only simulations and found that the flux density estimates of the sources converged to within 1% of their simulation values before the 25th iteration of the preconditioned conjugate gradient map solver (see Fowler et al. 2010 for a fuller description of the solver). This study uses a map from the 100th iteration of the ACT maps. Therefore, we conclude that the flux densities are not biased by failure of the mapping algorithm convergence.

3.3. Purity and Completeness

The number of false detections in our catalog of 157 sources is estimated by running the detection algorithm on an inverted (negative temperature) map in which the SZ decrements from all ACT-detected and optically confirmed clusters have been masked. A full description of the ACT SZ cluster population and optical follow-up can be found in Menanteau et al. (2010). With this approach, three spurious detections are found, giving a purity of 98% for detections above an S/N of 5.25. Below this S/N , the purity of the sample was found to decrease rapidly with only $\sim 50\%$ purity in the range $5 < S/N < 5.25$ (seven false detections). These results are consistent with estimates of purity based on cross-identification of the ACT detections with other catalogs (see Section 4.1). From simple Gaussian statistics, one expects fewer than five false detections in a sample selected with $S/N > 5$. Thus, some fraction of the false detections are may be the result of localized noise not accounted for by the weighting and matched filter.

Simulations from Sehgal et al. (2010) with noise from difference maps (see Section 2.3) were used to estimate completeness. Table 1 summarizes the findings. Due primarily to the uneven depth of coverage, the population of sources detected between 15 and 20 mJy was found on average to be 86% complete and the population between 20 and 30 mJy to be 97% complete. Because of the strict 50 mJy lower bound set for detections in areas of the map characterized by integration times below 7 minutes, the 50–90 mJy range also suffers from an incompleteness of 94%. The full simulations of Sehgal et al. (2010) include a correlation between radio sources and galaxy clusters, and we have excluded the SZ component in order to simplify the current study. At 148 GHz, clusters manifest themselves as arcminute-scale temperature decrements in the map which will cancel source flux in superposed source–cluster pairs. We also ran the test described here with the SZ component from Sehgal et al. (2010) included in the simulations. The resulting cancellation of source flux density by cluster decrements was found to cause an additional few percent of the incompleteness in the source population with flux densities below 30 mJy.

Table 1
Number Counts, Purity, and Completeness^a

Flux Range (mJy)	Det	False	Completeness (%)	Area ^b (deg ²)
1390–2870	1	0	100	432
650–1390	1	0	100	432
330–650	2	0	100	432
170–330	4	0	100	432
90–170	12	0	100	432
50–90	22	0	94 ± 6	432
30–50	40	0	100	368
20–30	44	1 ± 1	97 ± 2	368
15–20	25	2 ± 1	86 ± 5	368

Notes.

^a See Figure 10 for a graph of purity/completeness-corrected differential source counts.

^b For a discussion of flux density-dependent area, see Section 2.4.

4. DISCUSSION

4.1. Comparison to Other Source Catalogs

As a first step in ACT source characterization we consider cross-identifications with other catalogs. Matches are established within a 30'' radius about an ACT source. The choice of association radius was made based on the positional rms of the ACT catalog and comparison catalogs (allowing for outliers) as well as the fact that the source of low-frequency radio signals in a given system may be physically displaced from the source of high-frequency radio signal. A general search through the NASA/IPAC Extragalactic Database finds that 31 ACT sources have measured redshifts, ranging from 0.003 to 2.46. In what follows, we consider in more detail several catalogs of particular relevance to the 148 GHz source population.

Of our 157 sources, 109 match sources in the 5, 8, and 20 GHz AT20G catalog. There are 180 AT20G sources in the survey area such that a random cross-identification would occur once in roughly 11600 cases.³⁵ The AT20G catalog is incomplete below 100 mJy (Murphy et al. 2010). Given that nearly all the radio sources detected at 148 GHz are expected to have relatively flat spectra (e.g., Vieira et al. 2010), faint ACT sources may not have matches in AT20G (see Section 4.3). We have proposed for time on the Australia Telescope Compact Array to measure flux densities for sources in the ACT catalog that do not appear in AT20G.

All but six of the ACT sources are co-located within 30'' of sources from AT20G or the 0.84 GHz SUMSS catalog (Mauch et al. 2003). Within our survey area, the sample of 14030 SUMSS sources is complete to 8 mJy. A random cross-identification with a SUMSS detection is a 1-in-150 event and thus a spurious SUMSS association is likely. Of the six ACT sources without cross-identification in AT20G or SUMSS, two (ACT-S J011830–511521, ACT-S J033133–515349) are within 50'' of a SUMSS source, and the former is relatively bright with a 148 GHz flux density of 47.6 mJy. Furthermore, a preliminary reduction of the ACT 218 GHz data identifies one of the remaining four (ACT-S J031823–533148) as a 5 σ detection. ACT-S J034157–515140, ACT-S J004042–511830, and ACT-S J035343–534553 have no match in the auxiliary catalogs and may be false detections. This number of false

detections is consistent with the study of sample purity presented in Section 3.3.

Comparing to the recently reported 2.0 mm measurements from the SPT (Vieira et al. 2010), we find 24 cross-identifications with ACT sources. The Vieira et al. (2010) study used a square survey of 87 deg² centered at 05 h right ascension. As such, the ACT and SPT surveys have only fractional overlap. Nevertheless, 2304 of the 3496 SPT source candidates (S/N > 3) fall within the ACT survey. All 24 matching sources were categorized in Vieira et al. (2010) as synchrotron-dominated.

Finally, we compare the ACT catalog to the Infrared Astronomical Satellite Point Source Catalog (IRAS PSC; Helou & Walker 1988). Three of the detections, ACT-S J041959–545622 (NGC 1566), ACT-S J04285–542959, and ACT-S J033133–515352 (IC 1954), are identified with sources in the IRAS PSC. All three sources display lower frequency radio emission and have been identified in the preliminary ACT 218 GHz analysis.

4.2. Correlation with X-ray Clusters

Radio-loud AGNs are frequently found in Brightest Cluster Galaxies (BCGs). From a study of radio-loud AGNs in the Sloan Digital Sky Survey (SDSS) using data from the National Radio Astronomy Observatory Very Large Array Sky Survey (Condon et al. 1998) and the Faint Images of the Radio Sky At Twenty Centimeters survey (Becker et al. 1995), Best et al. (2007) found that the probability of a BCG hosting a radio-loud AGN is significantly enhanced compared to field galaxies of the same stellar mass. Lin & Mohr (2007) found that the fraction of BCGs being radio-loud is higher compared to that of cluster galaxies of similar luminosity. This enhancement of radio activity is probably due to the fact that BCGs are located in special places—the centers of clusters—and the AGN activity is likely fueled by gas cooling, or due to galaxy interactions in these high-density regions.

We performed a simple check to test whether any of the ACT 148 GHz sources were associated with clusters by cross matching against the REFLEX catalog (Böhringer et al. 2004), which is a homogeneous, X-ray-selected sample with a nominal (0.1–2.4 keV) flux limit of $\gtrsim 3 \times 10^{-12}$ erg s⁻¹ covering $\delta < +2.5$ deg. The REFLEX catalog is >90% complete above its nominal flux limit, and 23 REFLEX clusters are located within the 2008 ACT survey region, spanning the redshift range $0.03 < z < 0.34$. Using a generous 5' matching radius, we find that three ACT sources are associated with REFLEX clusters: ACT-S J062142–524136 (RXC J0621.7–5242); ACT-S J042906–534943 (RXC J0429.1–5350/AS0463); and ACT-S J062620–534136 (RXC J0626.3–5341/A3391). The separation between the ACT sources and the corresponding REFLEX cluster positions is 0.3–1'. All of these clusters are at very low redshift (0.041–0.055), and have low masses ($\sim (0.4 - 2) \times 10^{14} M_{\odot}$, inferred from their X-ray luminosities).

All three of these ACT sources have corresponding matches in the AT20G catalog. For ACT-S J062142–524136, both the ACT and AT20G sources are located within < 5'' of each other and are coincident with the BCG, from inspection of DSS imaging. For the other two sources, we find that either the ACT source position (in the case of RXC J0626.3–5341) or the AT20G position (in the case of RXC J0429.1–5350) is coincident with the BCG, although the AT20G and ACT positions are offset by < 19''. In all cases, the projected radial distance between the BCG and the REFLEX X-ray position is < 60 kpc.

³⁵ This rough statistic estimates the probability of a spurious detection in the ACT data falling in the fractional area ($N \times \pi \times 30''^2$) occupied by the N sources from the auxiliary catalog.

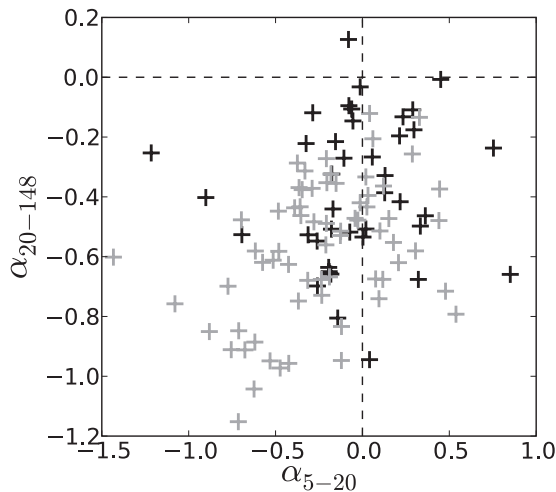


Figure 8. Radio source spectral indices. In this radio color–color diagram, 5–20 GHz and 20–148 GHz spectral indices are shown for ACT-AT20G cross-identified sources. The population is dominated by sources which are peaked (lower right quadrant) or falling (lower left quadrant). Black (gray) crosses correspond to sources with 148 GHz flux density greater (less) than 50 mJy. The low flux sample is incomplete and suffers from selection bias that favors sources with more negative spectral indices.

4.3. Source Spectra

It is established that radio source spectra extending to 148 GHz are not well characterized by a simple power law $S(\nu) \propto \nu^\alpha$ (e.g., de Zotti et al. 2010). Murphy et al. (2010) used a color–color comparison of spectral indices at 5–8 GHz and 8–20 GHz to show that the AT20G population may be decomposed into classical steep (and steepening) spectrum sources, sources that peak between their bands, and sources that show flat, rising or up-turned spectra. Following this example we construct a color–color comparison of 5–20 GHz and 20–148 GHz measurements, where the 5 and 20 GHz flux densities are from AT20G. The variability of these sources makes a per-source comparison difficult, but a study using the 109 ACT-AT20G cross-identifications as an ensemble is meaningful. Figure 8 is the α_{5-20} versus α_{20-148} color–color diagram. The figure shows that the ACT-AT20G cross-identified sources are predominantly characterized by spectral steepening. The sample is biased toward steepened spectra at low flux density ($S_{148} < 50$ mJy) due to incompleteness in AT20G.

The population can be further divided according to the 148 GHz flux density. In Figure 8, the black crosses correspond to the 42 brightest sources in the ACT sample and the gray crosses correspond to the faint half. The dividing flux density, 50 mJy, was chosen such that all but two of the ACT detections in the brighter sample have cross-identifications in AT20G. As described in Section 4.1, below this flux density the mean spectral indices of the population of ACT-AT20G cross-identified sources are biased negative by the incompleteness in AT20G below 100 mJy. The two sources in this high-flux subset which do not have AT20G counterparts are characterized by 150 GHz flux densities close to the 50 mJy cutoff and may have flatter spectra than the sample average. Including two extra sources with $\alpha = 0$ changes the mean spectral indices by $\sim 25\%$ of the statistical error, and therefore we simply use the 40 sources with AT20G counterparts in the following analysis. Considering only the unbiased, bright half of the distribution, the average spectrum steepens between 5–20 GHz and 20–148 GHz. The median spectral indices of the unbi-

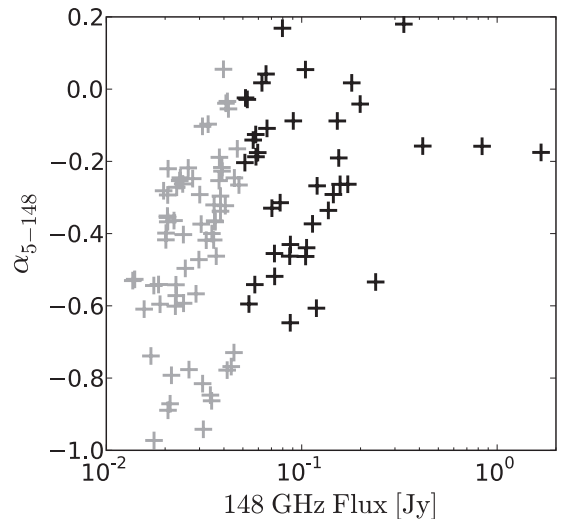


Figure 9. Radio color–magnitude diagram. As in Figure 8, the data are divided between high-flux densities (black crosses) and low-flux densities (gray crosses) at 50 mJy. The unbiased 50 mJy sample has a 5–148 GHz spectral index of $\alpha_{5-148} = -0.20 \pm 0.21(\pm 0.03)$. The low-flux density data suffer a selection bias that excludes sources with flat or rising spectra.

ased sample of sources are $\alpha_{5-20} = -0.07 \pm 0.37(\pm 0.06)$ and $\alpha_{20-148} = -0.39 \pm 0.24(\pm 0.04)$.³⁶ In obtaining the spectral indices we compare the deboosted flux densities from ACT with the raw flux densities from AT20G. Using the raw AT20G should not significantly bias the index estimates because the AT20G detections are all characterized by an S/N greater than 15.

When restricted to the unbiased sample with flux densities above 50 mJy, the 5–148 GHz spectral index is $\alpha_{5-148} = -0.20 \pm 0.21(\pm 0.03)$. This distribution is in 2.5σ tension with the SPT-reported mean 5–150 GHz spectral slope (for 57 sources) of $\alpha_{5-150} = -0.13 \pm 0.21(\pm 0.03)$ (Vieira et al. 2010).³⁷ Vieira et al. (2010) claim that the mean spectral index of the synchrotron-dominated species remains near -0.1 to 2.0 mm (≈ 148 GHz) after which it steepens such that the average slope between 2 mm and 1.4 mm (≈ 220 GHz) is -0.5 . This study suggests that the transition to the steep spectrum is more gradual. In fact, the spectral slope $\alpha_{20-148} = -0.39 \pm 0.24(\pm 0.04)$ approaches the -0.5 slope between 2.0 mm and 1.4 mm reported in Vieira et al. (2010). This picture is further supported by the rescaling of ACT 148 GHz source counts relative to source counts at 30 GHz (see Section 4.4). Figure 9 shows the ACT 5–148 GHz spectral indices as a function of flux density. The low flux density sample, represented by gray crosses, is incomplete for high spectral indices. Follow-up of the 148 GHz selected sources without matches in AT20G will complete the picture in the range 20–50 mJy.

4.4. Source Counts

The differential number counts for ACT sources based on data in Table 1 are plotted in Figure 10. The figure shows that the ACT counts are fit reasonably well by the model for radio sources from Toffolatti et al. (1998) scaled by a factor of 0.34 ± 0.04 . Depending on whether the rescaling is fit to the data in log or linear coordinates the best-fit value varies from 0.31 to 0.35. As in Figure 10, we adopt the rescaling of 0.34

³⁶ The errors on spectral indices are the 68% confidence levels of the distribution and, in parentheses, for the median.

³⁷ Note the tension arises for the center of the spectral index distribution which is better constrained than the index of any given source.

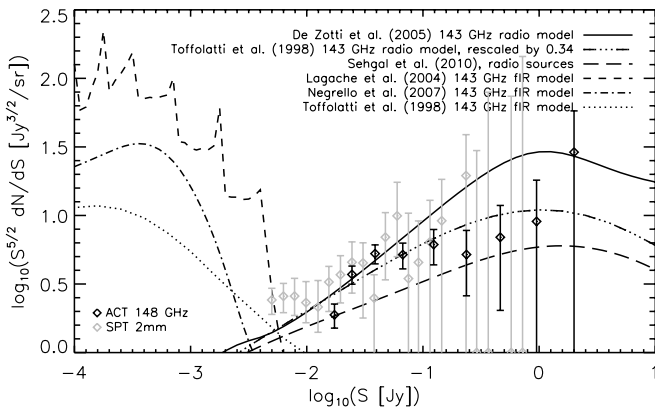


Figure 10. 148 GHz differential source counts. Derived from Table 1 and corrected for completeness, the ACT differential source counts (bold diamonds) are plotted together with models of radio and infrared source populations at 143 GHz (as computed for the 2 mm band of the Planck satellite). The data are consistent with being dominated by radio sources. Data (gray diamonds) from the SPT (Vieira et al. 2010) are consistent with the ACT counts. Errors (1σ) are Poissonian.

which lies between these two values. The ACT results are also consistent with counts reported by the SPT (Vieira et al. 2010). As part of the *WMAP* 7 year analysis, Wright et al. (2009) fit differential source counts at 30 GHz from *WMAP*, the Very Small Array (Cleary et al. 2006), Cosmic Background Imager (Mason et al. 2003), and DASI (Kovac et al. 2002). They found that the best-fit scaling for the Toffolatti et al. (1998) model at 30 GHz is 0.64. This result was also consistent with 30 GHz measurements by the Sunyaev Zel’dovich Array which covered a fainter range of flux densities (Muchovej et al. 2010). The apparent discrepancy between the 30 GHz and 148 GHz scalings can be explained by the steepening of the radio source spectrum described in Section 4.3. The source count model traditionally adopted from Toffolatti et al. (1998) uses an average spectral index of $\alpha = 0$ for radio sources between 20 and 200 GHz. From the unbiased sample of spectral indices (dark crosses) in Figure 8, the slope between 20 and 148 GHz is $\alpha \approx -0.4$. As can be seen from Figure 10, the radio source number counts are well approximated by a power law $N(>S) \propto S^{-1}$ between 0.01 and 1 Jy ($dN/dS S^{5/2} \propto S^{1/2}$). It follows that the 148 GHz number counts should be rescaled by

$$\begin{aligned} 0.64 \times \frac{S_{148\text{GHz}}}{S_{30\text{GHz}}} &\approx 0.64 \times \left(\frac{148\text{GHz}}{30\text{GHz}}\right)^\alpha & (9) \\ &\approx 0.64 \times 5^{-0.4} \\ &\approx 0.35, \end{aligned}$$

consistent with the scaling of Toffolatti et al. (1998) to the ACT data. Also shown in the plot are radio source models from De Zotti et al. (2005) and Sehgal et al. (2010). The De Zotti et al. (2005) model is consistent with the ACT source counts at low flux densities ($S < 0.1$ Jy) and overpredicts the counts at higher flux densities. The model presented in Sehgal et al. (2010), although underestimating the source counts at $S < 0.1$ Jy, seems to be consistent with ACT data at higher fluxes.

Differential source counts derived from the 150 GHz catalog from ACBAR (Reichardt et al. 2009) are consistent with Toffolatti et al. (1998) scaled by 0.64. However, ACBAR’s resolution and sensitivity made it sensitive to only the brightest sources with flux densities mainly in excess of 100 mJy where there are fewer sources. Furthermore, the ACBAR fields were chosen specifically to have bright quasars for beam measure-

ment (Kuo et al. 2007) such that the differential source counts derived from the ACBAR data are biased high. The ACT field was chosen with no a priori knowledge of source population. Allowing for variability, there is reasonable agreement in the flux densities reported by ACBAR and ACT for the seven sources common to both catalogs.

Also shown in Figure 10 are models for counts of dusty starburst galaxies (Toffolatti et al. 1998; Lagache et al. 2004; Negrello et al. 2007). The brightest infrared sources in these models are 10 mJy. Given that all sources in the ACT catalog have flux densities greater than 10 mJy, these models predict that the 148 GHz-selected ACT catalog should have few or no infrared sources.

4.5. Contribution to the Power Spectrum

The $\ell = 3000$ –10000 power spectrum of the 148 GHz sky is dominated by synchrotron and infrared sources as well as the thermal SZ from clusters (Hall et al. 2010; Fowler et al. 2010). In particular, the power spectrum at the highest multipoles constrains the Poisson distributed component of the source population, and an understanding of the residual synchrotron population helps break the high- ℓ spectral degeneracy between synchrotron and infrared sources. The contribution to the power spectrum by a Poisson-distributed population of sources is a function of the number counts:

$$C^{\text{PS}} = \left(\frac{\delta B_{\nu}}{\delta T}\right)^{-2} \int_0^{S_{\text{lim}}} S^2 \frac{dN}{dS} dS, \quad (10)$$

where S_{lim} is the upper-limiting flux density of the residual (i.e., unmasked) sources in the data. With a limiting flux density of 20 mJy and the rescaled model of Toffolatti et al. (1998) from Section 4.4, one expects a synchrotron contribution to the Poisson power spectrum of $C^{\text{Synch}} = (2.8 \pm 0.3) \times 10^{-6} \mu\text{K}^2$.

Fowler et al. (2010) used a 20 mJy cut for masking sources and found a Poisson spectrum from all residual sources of $C^{\text{PS}} = (7.8 \pm 2.3) \times 10^{-6} \mu\text{K}^2$. Thus from this study we expect an infrared contribution to the Poisson spectrum of $C^{\text{IR}} = (5.0 \pm 2.3) \times 10^{-6} \mu\text{K}^2$. A similar argument applied to the study of Lueker et al. (2010) results in an estimate of the residual Poisson term for infrared sources of $C^{\text{IR}} \approx (6.3 \pm 0.5) \times 10^{-6} \mu\text{K}^2$. Thus, within the Fowler et al. (2010) errors, the two studies of the high- ℓ power spectrum at 148 GHz are consistent.

5. CONCLUSIONS

We have presented results on extragalactic sources at 148 GHz from data taken by ACT during the 2008 observing season. A catalog of 157 millimeter sources has been presented with sources detected across two decades in flux density, from 15 mJy to 1500 mJy. The flux density calibration of the sources derives from observations of Uranus with 6% error. Bias in the quoted flux densities due to beam shape uncertainty is estimated at less than 1%. Typical statistical 1σ errors for the source flux density range from 2.5 mJy to 5 mJy. The catalog astrometry error for the brightest sources is characterized by an rms of $3''.5$. The catalog is estimated to be 98% pure and complete above 20 mJy.

Comparison to other catalogs shows that 98% of the ACT detections correspond to sources detected at lower radio frequencies. The differential source counts are also consistent with the finding that ACT detections correspond to sources detected

Table A1
ACT High Significance 148 GHz Extragalactic Source Catalog

ACT ID	R.A. (J2000) Decl.		S/N	S_m^a	S_{db}^b	t_{int}^c	AT20G ID
	(hms)	($^{\circ}$ $'$ $''$)					
ACT-S J001850–511454	00 : 18 : 50	–51 : 14 : 54	10.4	53.7	$53.7^{+5.2}_{-5.2}$	6.1	AT20G J001849–511455
ACT-S J001851–492949	00 : 18 : 51	–49 : 29 : 49	7.4	52.8	$52.8^{+7.1}_{-7.1}$	3.0	...
ACT-S J002513–542737	00 : 25 : 13	–54 : 27 : 37	6.7	26.1	$24.8^{+3.9}_{-4.0}$	10.0	AT20G J002511–542739
ACT-S J003134–514308	00 : 31 : 34	–51 : 43 : 08	13.9	52.7	$52.7^{+3.8}_{-3.8}$	10.3	AT20G J003134–514325
ACT-S J003734–530729	00 : 37 : 34	–53 : 07 : 29	11.9	39.1	$38.5^{+3.3}_{-3.3}$	13.9	AT20G J003735–530733
ACT-S J004012–514950	00 : 40 : 12	–51 : 49 : 50	5.7	20.2	$18.7^{+3.7}_{-3.7}$	12.2	...
ACT-S J004042–511830	00 : 40 : 42	–51 : 18 : 30	5.6	22.9	$21.1^{+4.2}_{-4.2}$	9.5	...
ACT-S J004906–552106	00 : 49 : 06	–55 : 21 : 06	14.1	62.6	$62.6^{+4.5}_{-4.5}$	7.5	AT20G J004905–552110
ACT-S J004949–540240	00 : 49 : 49	–54 : 02 : 40	6.7	21.8	$20.7^{+3.3}_{-3.3}$	14.2	...
ACT-S J005240–531127	00 : 52 : 40	–53 : 11 : 27	5.5	17.6	$16.2^{+3.4}_{-3.4}$	14.5	...
ACT-S J005605–524154	00 : 56 : 05	–52 : 41 : 54	8.2	28.6	$27.6^{+3.5}_{-3.5}$	12.5	...
ACT-S J005622–531845	00 : 56 : 22	–53 : 18 : 45	9.7	32.4	$31.6^{+3.4}_{-3.4}$	13.5	...
ACT-S J005706–521423	00 : 57 : 06	–52 : 14 : 23	13.9	47.4	$46.8^{+3.4}_{-3.4}$	12.7	AT20G J005705–521418
ACT-S J005855–521925	00 : 58 : 55	–52 : 19 : 25	20.3	70.4	$70.4^{+3.5}_{-3.5}$	12.4	AT20G J005855–521926
ACT-S J010309–510907	01 : 03 : 09	–51 : 09 : 07	8.8	33.5	$32.5^{+3.8}_{-3.8}$	10.4	AT20G J010306–510907
ACT-S J010330–513544	01 : 03 : 30	–51 : 35 : 44	11.7	41.9	$41.2^{+3.6}_{-3.6}$	12.0	AT20G J010329–513551
ACT-S J011324–532938	01 : 13 : 24	–53 : 29 : 38	7.2	22.4	$21.4^{+3.2}_{-3.2}$	15.4	AT20G J011323–532949
ACT-S J011654–544653	01 : 16 : 54	–54 : 46 : 53	5.8	21.0	$19.5^{+3.7}_{-3.8}$	11.3	...
ACT-S J011830–511521	01 : 18 : 30	–51 : 15 : 21	13.0	48.4	$47.7^{+3.6}_{-3.7}$	11.0	...
ACT-S J011950–535714	01 : 19 : 50	–53 : 57 : 14	46.9	157.2	$157.2^{+3.4}_{-3.4}$	15.4	AT20G J011950–535717
ACT-S J012006–521104	01 : 20 : 06	–52 : 11 : 04	6.1	19.6	$18.4^{+3.3}_{-3.3}$	14.8	AT20G J012008–521102
ACT-S J012457–511309	01 : 24 : 57	–51 : 13 : 09	51.0	199.1	$199.1^{+3.9}_{-3.9}$	11.4	AT20G J012457–511316
ACT-S J012501–532514	01 : 25 : 01	–53 : 25 : 14	5.3	15.5	$14.2^{+3.1}_{-3.2}$	17.6	...
ACT-S J012623–510305	01 : 26 : 23	–51 : 03 : 05	7.0	26.0	$24.8^{+3.8}_{-3.8}$	11.1	AT20G J012624–510309
ACT-S J012755–513642	01 : 27 : 55	–51 : 36 : 42	12.1	39.5	$38.8^{+3.3}_{-3.3}$	14.1	AT20G J012756–513641
ACT-S J012756–532933	01 : 27 : 56	–53 : 29 : 33	9.6	27.6	$26.9^{+2.9}_{-2.9}$	18.1	...
ACT-S J012834–525520	01 : 28 : 34	–52 : 55 : 20	6.3	18.5	$17.4^{+3.0}_{-3.0}$	17.7	AT20G J012834–525519
ACT-S J013107–545707	01 : 31 : 07	–54 : 57 : 07	6.3	23.8	$22.3^{+3.9}_{-3.9}$	10.3	...
ACT-S J013225–512903	01 : 32 : 25	–51 : 29 : 03	5.3	18.4	$16.8^{+3.6}_{-3.7}$	12.9	...
ACT-S J013306–520003	01 : 33 : 06	–52 : 00 : 03	74.7	239.0	$239.0^{+3.2}_{-3.2}$	17.1	AT20G J013305–520003
ACT-S J013409–552612	01 : 34 : 09	–55 : 26 : 12	6.0	24.7	$23.1^{+4.2}_{-4.3}$	8.8	AT20G J013408–552616
ACT-S J013541–514943	01 : 35 : 41	–51 : 49 : 43	6.6	19.8	$18.8^{+3.0}_{-3.1}$	16.7	AT20G J013540–514945
ACT-S J013548–524414	01 : 35 : 48	–52 : 44 : 14	18.2	51.6	$51.6^{+2.8}_{-2.8}$	18.8	AT20G J013548–524417
ACT-S J013727–543942	01 : 37 : 27	–54 : 39 : 42	7.4	25.3	$24.2^{+3.5}_{-3.5}$	12.6	...
ACT-S J013949–521739	01 : 39 : 49	–52 : 17 : 39	12.1	35.2	$34.6^{+2.9}_{-2.9}$	17.7	AT20G J013949–521746
ACT-S J014648–520232	01 : 46 : 48	–52 : 02 : 32	25.3	77.5	$77.5^{+3.1}_{-3.1}$	16.0	AT20G J014648–520233
ACT-S J015358–540649	01 : 53 : 58	–54 : 06 : 49	11.4	33.7	$33.1^{+3.0}_{-3.0}$	16.9	AT20G J015358–540653
ACT-S J015420–510750	01 : 54 : 20	–51 : 07 : 50	49.3	172.1	$172.1^{+3.5}_{-3.5}$	14.2	AT20G J015419–510751
ACT-S J015559–512538	01 : 55 : 59	–51 : 25 : 38	5.8	18.2	$16.9^{+3.2}_{-3.3}$	15.0	AT20G J015557–512545
ACT-S J015649–543940	01 : 56 : 49	–54 : 39 : 40	13.4	42.2	$41.6^{+3.2}_{-3.2}$	15.1	AT20G J015649–543949
ACT-S J015817–500415	01 : 58 : 17	–50 : 04 : 15	5.8	24.6	$22.8^{+4.4}_{-4.4}$	8.3	AT20G J015817–500419
ACT-S J015914–530902	01 : 59 : 14	–53 : 09 : 02	9.2	25.3	$24.7^{+2.8}_{-2.8}$	19.8	AT20G J015913–530853
ACT-S J020448–550257	02 : 04 : 48	–55 : 02 : 57	14.7	48.4	$47.9^{+3.2}_{-3.3}$	13.6	...
ACT-S J020649–534528	02 : 06 : 49	–53 : 45 : 28	5.4	15.2	$13.9^{+2.9}_{-3.0}$	19.4	AT20G J020647–534543
ACT-S J020920–522921	02 : 09 : 20	–52 : 29 : 21	11.1	30.5	$29.9^{+2.8}_{-2.8}$	20.2	...
ACT-S J021046–510100	02 : 10 : 46	–51 : 01 : 00	470.3	1677.6	$1678.0^{+3.6}_{-3.6}$	13.6	AT20G J021046–510101
ACT-S J021519–510435	02 : 15 : 19	–51 : 04 : 35	5.5	17.3	$15.9^{+3.3}_{-3.4}$	15.1	...
ACT-S J021603–520007	02 : 16 : 03	–52 : 00 : 07	12.7	34.6	$34.1^{+2.7}_{-2.7}$	20.1	AT20G J021603–520012
ACT-S J021709–542750	02 : 17 : 09	–54 : 27 : 50	5.8	17.3	$16.1^{+3.1}_{-3.1}$	16.4	...
ACT-S J021835–550354	02 : 18 : 35	–55 : 03 : 54	12.5	43.0	$42.4^{+3.5}_{-3.5}$	12.5	AT20G J021834–550350
ACT-S J022216–510627	02 : 22 : 16	–51 : 06 : 27	9.4	29.7	$28.9^{+3.2}_{-3.2}$	15.1	AT20G J022215–510629
ACT-S J022330–534737	02 : 23 : 30	–53 : 47 : 37	40.5	119.9	$119.9^{+3.0}_{-3.0}$	19.4	AT20G J022330–534740
ACT-S J022530–522547	02 : 25 : 30	–52 : 25 : 47	15.3	40.2	$39.8^{+2.6}_{-2.7}$	21.4	AT20G J022529–522555

Table A1
(Continued)

ACT ID	R.A. (J2000) Decl.		S/N	S_m^a	S_{db}^b	t_{int}^c	AT20G ID
	(hms)	($^{\circ}$ / $'$ / $''$)					
ACT-S J022820–553732	02 : 28 : 20	–55 : 37 : 32	5.6	21.9	20.2 ^{+4.1} _{–4.1}	9.8	AT20G J022820–553725
ACT-S J022821–554601	02 : 28 : 21	–55 : 46 : 01	25.9	104.7	104.7 ^{+4.0} _{–4.0}	9.0	AT20G J022821–554603
ACT-S J022912–540324	02 : 29 : 12	–54 : 03 : 24	112.5	333.1	333.1 ^{+3.0} _{–3.0}	19.9	AT20G J022912–540324
ACT-S J022925–523226	02 : 29 : 25	–52 : 32 : 26	17.2	45.3	44.9 ^{+2.6} _{–2.6}	21.7	AT20G J022925–523226
ACT-S J023245–535634	02 : 32 : 45	–53 : 56 : 34	8.1	21.9	21.2 ^{+2.7} _{–2.7}	20.7	...
ACT-S J023357–503014	02 : 33 : 57	–50 : 30 : 14	6.3	21.4	20.2 ^{+3.5} _{–3.5}	13.0	AT20G J023356–503020
ACT-S J023924–510824	02 : 39 : 24	–51 : 08 : 24	8.5	25.2	24.4 ^{+3.0} _{–3.0}	16.8	...
ACT-S J024040–542942	02 : 40 : 40	–54 : 29 : 42	6.9	21.7	20.7 ^{+3.2} _{–3.2}	15.3	AT20G J024040–542933
ACT-S J024154–534541	02 : 41 : 54	–53 : 45 : 41	6.7	17.8	16.9 ^{+2.7} _{–2.8}	20.9	...
ACT-S J024313–510512	02 : 43 : 13	–51 : 05 : 12	11.5	35.1	34.5 ^{+3.1} _{–3.1}	16.2	AT20G J024313–510517
ACT-S J024539–525756	02 : 45 : 39	–52 : 57 : 56	7.6	19.1	18.4 ^{+2.6} _{–2.6}	23.4	...
ACT-S J024614–495346	02 : 46 : 14	–49 : 53 : 46	10.3	42.8	41.9 ^{+4.2} _{–4.2}	8.5	AT20G J024614–495350
ACT-S J024947–555619	02 : 49 : 47	–55 : 56 : 19	5.4	22.8	20.9 ^{+4.4} _{–4.6}	8.2	AT20G J024948–555615
ACT-S J025112–520822	02 : 51 : 12	–52 : 08 : 22	5.7	15.0	13.9 ^{+2.7} _{–2.8}	21.8	...
ACT-S J025204–514554	02 : 52 : 04	–51 : 45 : 54	5.4	14.4	13.2 ^{+2.8} _{–2.8}	20.7	...
ACT-S J025328–544151	02 : 53 : 28	–54 : 41 : 51	246.7	837.5	837.5 ^{+3.4} _{–3.4}	15.3	AT20G J025329–544151
ACT-S J025629–522711	02 : 56 : 29	–52 : 27 : 11	5.3	14.1	12.8 ^{+2.8} _{–2.9}	21.0	...
ACT-S J025838–505200	02 : 58 : 38	–50 : 52 : 00	33.2	113.6	113.6 ^{+3.4} _{–3.4}	14.6	AT20G J025838–505204
ACT-S J025849–533210	02 : 58 : 49	–53 : 32 : 10	7.2	19.5	18.6 ^{+2.7} _{–2.8}	20.6	...
ACT-S J030056–510229	03 : 00 : 56	–51 : 02 : 29	11.2	36.8	36.1 ^{+3.3} _{–3.3}	14.0	AT20G J030055–510229
ACT-S J030132–525603	03 : 01 : 32	–52 : 56 : 03	15.0	39.7	39.3 ^{+2.6} _{–2.7}	21.6	...
ACT-S J030327–523427	03 : 03 : 27	–52 : 34 : 27	24.8	66.4	66.4 ^{+2.7} _{–2.7}	21.0	AT20G J030328–523433
ACT-S J030616–552808	03 : 06 : 16	–55 : 28 : 08	15.2	56.4	56.5 ^{+3.7} _{–3.7}	10.9	AT20G J030616–552808
ACT-S J031206–554135	03 : 12 : 06	–55 : 41 : 35	18.3	72.7	72.7 ^{+4.0} _{–4.0}	9.5	AT20G J031207–554133
ACT-S J031426–510430	03 : 14 : 26	–51 : 04 : 30	29.0	90.6	90.5 ^{+3.1} _{–3.1}	15.2	AT20G J031425–510431
ACT-S J031823–533148	03 : 18 : 23	–53 : 31 : 48	18.6	51.6	51.6 ^{+2.8} _{–2.8}	19.6	...
ACT-S J031910–500031	03 : 19 : 10	–50 : 00 : 31	7.5	30.2	28.9 ^{+4.1} _{–4.1}	9.3	...
ACT-S J032207–535419	03 : 22 : 07	–53 : 54 : 19	6.5	18.3	17.3 ^{+2.9} _{–2.9}	19.6	...
ACT-S J032212–504229	03 : 22 : 12	–50 : 42 : 29	11.0	35.5	34.8 ^{+3.2} _{–3.3}	14.5	...
ACT-S J032327–522627	03 : 23 : 27	–52 : 26 : 27	14.9	41.0	40.5 ^{+2.8} _{–2.8}	19.7	AT20G J032327–522630
ACT-S J032650–533658	03 : 26 : 50	–53 : 36 : 58	17.0	48.0	47.6 ^{+2.8} _{–2.8}	18.9	AT20G J032650–533701
ACT-S J033002–503518	03 : 30 : 02	–50 : 35 : 18	6.5	21.9	20.7 ^{+3.4} _{–3.4}	13.5	AT20G J033002–503519
ACT-S J033114–524149	03 : 31 : 14	–52 : 41 : 49	9.0	24.4	23.7 ^{+2.7} _{–2.7}	21.1	AT20G J033114–524148
ACT-S J033126–525829	03 : 31 : 26	–52 : 58 : 29	11.9	31.6	31.0 ^{+2.7} _{–2.7}	21.5	AT20G J033126–525830
ACT-S J033133–515352	03 : 31 : 33	–51 : 53 : 52	5.9	16.1	15.0 ^{+2.8} _{–2.9}	19.8	...
ACT-S J033444–521851	03 : 34 : 44	–52 : 18 : 51	7.1	19.2	18.4 ^{+2.8} _{–2.8}	20.4	...
ACT-S J033554–543028	03 : 35 : 54	–54 : 30 : 28	14.8	44.0	43.6 ^{+3.0} _{–3.0}	16.6	AT20G J033553–543025
ACT-S J034157–515140	03 : 41 : 57	–51 : 51 : 40	6.3	16.6	15.7 ^{+2.7} _{–2.7}	22.1	...
ACT-S J034348–524112	03 : 43 : 48	–52 : 41 : 12	8.3	21.9	21.2 ^{+2.7} _{–2.7}	21.5	AT20G J034349–524116
ACT-S J034940–540111	03 : 49 : 40	–54 : 01 : 11	7.4	21.7	20.7 ^{+3.0} _{–3.0}	17.1	AT20G J034941–540106
ACT-S J035128–514254	03 : 51 : 28	–51 : 42 : 54	50.7	145.2	145.2 ^{+2.9} _{–2.9}	21.6	AT20G J035128–514254
ACT-S J035343–534553	03 : 53 : 43	–53 : 45 : 53	5.6	16.3	15.0 ^{+3.0} _{–3.1}	17.9	...
ACT-S J035700–495549	03 : 57 : 00	–49 : 55 : 49	14.1	58.3	58.3 ^{+4.1} _{–4.1}	8.7	AT20G J035700–495547
ACT-S J035840–543403	03 : 58 : 40	–54 : 34 : 03	8.3	27.4	26.4 ^{+3.3} _{–3.4}	14.0	...
ACT-S J040401–552022	04 : 04 : 01	–55 : 20 : 22	7.0	27.6	26.3 ^{+4.0} _{–4.0}	10.2	AT20G J040400–552023
ACT-S J040621–503509	04 : 06 : 21	–50 : 35 : 09	5.5	20.5	18.8 ^{+3.9} _{–4.0}	10.8	...
ACT-S J041137–514918	04 : 11 : 37	–51 : 49 : 18	22.8	72.5	72.5 ^{+3.2} _{–3.2}	14.9	AT20G J041137–514923
ACT-S J041247–560044	04 : 12 : 47	–56 : 00 : 44	5.4	23.4	21.4 ^{+4.5} _{–4.6}	8.1	AT20G J041247–560035
ACT-S J041313–533157	04 : 13 : 13	–53 : 31 : 57	13.2	39.5	38.9 ^{+3.0} _{–3.0}	16.6	AT20G J041313–533200
ACT-S J041959–545618	04 : 19 : 59	–54 : 56 : 18	7.2	23.8	22.7 ^{+3.4} _{–3.4}	13.8	...
ACT-S J042503–533201	04 : 25 : 03	–53 : 32 : 01	49.8	152.1	152.1 ^{+3.1} _{–3.1}	18.6	AT20G J042504–533158
ACT-S J042842–500532	04 : 28 : 42	–50 : 05 : 32	33.1	154.7	154.7 ^{+4.7} _{–4.7}	6.9	AT20G J042842–500534
ACT-S J042852–543001	04 : 28 : 52	–54 : 30 : 01	6.8	21.8	20.8 ^{+3.3} _{–3.3}	14.5	AT20G J042852–543007

Table A1
(Continued)

ACT ID	R.A. (J2000) Decl.		S/N	S_m^a (mJy)	S_{db}^b (mJy)	t_{int}^c (minutes)	AT20G ID
	(hms)	($^{\circ}$ / $'$ / $''$)					
ACT-S J042906–534943	04 : 29 : 06	–53 : 49 : 43	31.7	87.4	87.4 ^{+2.8} _{–2.8}	19.9	AT20G J042908–534940
ACT-S J043221–510926	04 : 32 : 21	–51 : 09 : 26	26.5	86.8	86.8 ^{+3.3} _{–3.3}	14.1	AT20G J043221–510925
ACT-S J043651–521632	04 : 36 : 51	–52 : 16 : 32	14.1	38.4	38.0 ^{+2.7} _{–2.7}	20.4	AT20G J043652–521639
ACT-S J044115–543848	04 : 41 : 15	–54 : 38 : 48	6.1	19.4	18.2 ^{+3.3} _{–3.3}	14.9	...
ACT-S J044158–515456	04 : 41 : 58	–51 : 54 : 56	30.4	87.5	87.5 ^{+2.9} _{–2.9}	18.2	AT20G J044158–515453
ACT-S J044502–523426	04 : 45 : 02	–52 : 34 : 26	9.1	25.5	24.8 ^{+2.8} _{–2.8}	19.4	...
ACT-S J044746–515103	04 : 47 : 46	–51 : 51 : 03	9.7	27.2	26.5 ^{+2.8} _{–2.8}	19.3	AT20G J044748–515100
ACT-S J044821–504140	04 : 48 : 21	–50 : 41 : 40	10.8	37.1	36.3 ^{+3.5} _{–3.4}	13.1	AT20G J044822–504133
ACT-S J045028–534659	04 : 50 : 28	–53 : 46 : 59	8.9	24.8	24.1 ^{+2.8} _{–2.8}	19.5	...
ACT-S J045103–493632	04 : 51 : 03	–49 : 36 : 32	12.1	58.2	58.2 ^{+4.8} _{–4.8}	6.3	AT20G J045102–493626
ACT-S J045239–530637	04 : 52 : 39	–53 : 06 : 37	8.4	23.3	22.6 ^{+2.8} _{–2.8}	19.3	AT20G J045238–530635
ACT-S J045503–553119	04 : 55 : 03	–55 : 31 : 19	9.8	36.7	35.8 ^{+3.8} _{–3.8}	10.8	AT20G J045503–553112
ACT-S J045559–530236	04 : 55 : 59	–53 : 02 : 36	6.9	18.3	17.4 ^{+2.7} _{–2.7}	21.2	AT20G J045558–530239
ACT-S J050018–532122	05 : 00 : 18	–53 : 21 : 22	10.6	28.2	27.6 ^{+2.7} _{–2.7}	21.3	AT20G J050019–532121
ACT-S J050401–502314	05 : 04 : 01	–50 : 23 : 14	15.8	59.6	59.5 ^{+3.8} _{–3.8}	10.7	AT20G J050401–502313
ACT-S J051355–505543	05 : 13 : 55	–50 : 55 : 43	6.5	22.0	20.9 ^{+3.4} _{–3.5}	13.4	AT20G J051355–505541
ACT-S J051812–514359	05 : 18 : 12	–51 : 43 : 59	8.7	24.7	23.9 ^{+2.9} _{–2.9}	18.6	AT20G J051811–514404
ACT-S J052044–550832	05 : 20 : 44	–55 : 08 : 32	7.0	24.1	22.9 ^{+3.5} _{–3.5}	12.7	AT20G J052045–550824
ACT-S J052317–530836	05 : 23 : 17	–53 : 08 : 36	8.4	22.9	22.1 ^{+2.7} _{–2.7}	20.5	AT20G J052318–530837
ACT-S J052743–542614	05 : 27 : 43	–54 : 26 : 14	8.9	26.0	25.3 ^{+2.9} _{–2.9}	17.3	AT20G J052743–542616
ACT-S J053117–550431	05 : 31 : 17	–55 : 04 : 31	14.1	47.9	47.3 ^{+3.3} _{–3.4}	13.0	...
ACT-S J053208–531035	05 : 32 : 08	–53 : 10 : 35	18.9	51.2	51.2 ^{+2.7} _{–2.7}	20.3	AT20G J053208–531035
ACT-S J053323–554941	05 : 33 : 23	–55 : 49 : 41	16.7	65.7	65.7 ^{+3.9} _{–3.9}	9.7	AT20G J053324–554936
ACT-S J053458–543903	05 : 34 : 58	–54 : 39 : 03	10.0	30.8	30.1 ^{+3.1} _{–3.1}	15.7	AT20G J053458–543901
ACT-S J053909–551059	05 : 39 : 09	–55 : 10 : 59	8.9	30.6	29.7 ^{+3.5} _{–3.5}	12.8	AT20G J053909–551059
ACT-S J054025–530354	05 : 40 : 25	–53 : 03 : 54	11.5	31.7	31.1 ^{+2.8} _{–2.8}	19.9	AT20G J054025–530346
ACT-S J054029–535628	05 : 40 : 29	–53 : 56 : 28	5.5	14.8	13.6 ^{+2.8} _{–2.8}	21.2	AT20G J054029–535632
ACT-S J054046–541825	05 : 40 : 46	–54 : 18 : 25	133.4	416.2	416.2 ^{+3.1} _{–3.1}	17.4	AT20G J054045–541821
ACT-S J054223–514259	05 : 42 : 23	–51 : 42 : 59	27.4	79.7	79.7 ^{+2.9} _{–2.9}	18.1	AT20G J054223–514257
ACT-S J054357–553206	05 : 43 : 57	–55 : 32 : 06	6.2	22.2	20.9 ^{+3.7} _{–3.7}	11.3	...
ACT-S J054830–521836	05 : 48 : 30	–52 : 18 : 36	9.3	25.2	24.6 ^{+2.7} _{–2.7}	20.2	...
ACT-S J054943–524629	05 : 49 : 43	–52 : 46 : 29	63.4	180.3	180.3 ^{+2.8} _{–2.8}	21.8	AT20G J054943–524625
ACT-S J055047–530502	05 : 50 : 47	–53 : 05 : 02	9.0	24.5	23.8 ^{+2.8} _{–2.8}	20.1	...
ACT-S J055152–552642	05 : 51 : 52	–55 : 26 : 42	8.6	31.5	30.4 ^{+3.7} _{–3.7}	11.1	AT20G J055152–552632
ACT-S J055811–502957	05 : 58 : 11	–50 : 29 : 57	16.0	57.5	57.5 ^{+3.6} _{–3.6}	11.8	AT20G J055811–502948
ACT-S J055830–532640	05 : 58 : 30	–53 : 26 : 40	6.1	16.6	15.6 ^{+2.8} _{–2.8}	19.7	AT20G J055830–532631
ACT-S J055946–502656	05 : 59 : 46	–50 : 26 : 56	12.5	45.9	45.2 ^{+3.7} _{–3.7}	11.2	AT20G J055947–502652
ACT-S J060213–542509	06 : 02 : 13	–54 : 25 : 09	12.5	38.3	37.7 ^{+3.1} _{–3.1}	15.9	AT20G J060212–542507
ACT-S J060749–525747	06 : 07 : 49	–52 : 57 : 47	13.1	36.0	35.5 ^{+2.8} _{–2.7}	19.6	AT20G J060749–525744
ACT-S J060849–545650	06 : 08 : 49	–54 : 56 : 50	38.4	136.9	136.9 ^{+3.6} _{–3.6}	13.7	AT20G J060849–545642
ACT-S J061715–530615	06 : 17 : 15	–53 : 06 : 15	13.1	39.6	39.0 ^{+3.0} _{–3.1}	16.2	...
ACT-S J061846–532948	06 : 18 : 46	–53 : 29 : 48	6.3	18.7	17.6 ^{+3.0} _{–3.1}	16.8	...
ACT-S J061955–542718	06 : 19 : 55	–54 : 27 : 18	12.1	39.1	38.5 ^{+3.3} _{–3.3}	13.8	AT20G J061955–542713
ACT-S J062142–524136	06 : 21 : 42	–52 : 41 : 36	37.3	118.9	118.9 ^{+3.2} _{–3.2}	17.4	AT20G J062143–524132
ACT-S J062552–543856	06 : 25 : 52	–54 : 38 : 56	28.5	105.9	105.9 ^{+3.7} _{–3.7}	10.8	AT20G J062552–543850
ACT-S J062620–534136	06 : 26 : 20	–53 : 41 : 36	15.1	46.7	46.3 ^{+3.1} _{–3.1}	15.8	AT20G J062620–534151
ACT-S J062649–543233	06 : 26 : 49	–54 : 32 : 33	8.9	32.8	31.8 ^{+3.7} _{–3.7}	11.0	AT20G J062648–543214
ACT-S J063200–540501	06 : 32 : 00	–54 : 05 : 01	6.1	21.0	19.7 ^{+3.5} _{–3.6}	12.7	AT20G J063201–540455
ACT-S J064111–520223	06 : 41 : 11	–52 : 02 : 23	5.8	19.4	18.1 ^{+3.4} _{–3.5}	13.5	...
ACT-S J064319–535850	06 : 43 : 19	–53 : 58 : 50	32.1	104.5	104.5 ^{+3.3} _{–3.3}	14.0	AT20G J064320–535846
ACT-S J064629–545120	06 : 46 : 29	–54 : 51 : 20	9.7	37.7	36.7 ^{+3.9} _{–3.9}	10.1	AT20G J064629–545116

Notes.^a Flux density as measured directly from the ACT 148 GHz map.^b Deboosted flux densities as described in Section 3.2.2 for sources with $S_m < 50$ mJy. For sources above 50 mJy, the measured flux together with S/N-derived errors is reported (see Section 3.2.2).^c Integration time per square arcminute.

at lower radio frequencies. In particular, the source counts are fit reasonably well by the radio model of Toffolatti et al. (1998) scaled by 0.34. This scaling, compared to a scaling 0.64 found at 30 GHz by Wright et al. (2009), suggests that the population of radio sources is characterized, on average, by spectral steepening between 30 GHz and 148 GHz. This conclusion is consistent with the average spectral indices derived from the combined AT20G and ACT data sets. Future work will address the more involved comparison with the De Zotti et al. (2005) and Sehgal et al. (2010) radio source models. With the rescaled model from Toffolatti et al. (1998) and a 20 mJy cut, the residual contribution of the synchrotron population to the Poisson power spectrum is $C^{\text{Sync}} = (2.8 \pm 0.3) \times 10^{-6} \mu\text{K}^2$.

Future ACT source work will incorporate the 218 GHz and 277 GHz bands, deeper coverage integrating the 2007, 2009, and (ongoing) 2010 seasons, as well as the equatorial survey overlapping the deep SDSS Stripe 82.

The ACT project was proposed in 2000 and funded by the U.S. National Science Foundation on 2004 January 1. Many have contributed to the project since its inception. We especially thank Asad Aboobaker, Christine Allen, Dominic Benford, Paul Bode, Kristen Burgess, Angelica de Oliveira-Costa, Peter Hargrave, Norm Jarosik, Amber Miller, Carl Reintsema, Felipe Rojas, Uros Seljak, Martin Spergel, Johannes Staguhn, Carl Stahle, Max Tegmark, Masao Uehara, Katerina Visnjic, and Ed Wishnow. It is a pleasure to acknowledge Bob Margolis, ACT's project manager. Reed Plimpton and David Jacobson worked at the telescope during the 2008 season. ACT is on the Chajnantor Science preserve, which was made possible by the Chilean Comisión Nacional de Investigación Científica y Tecnológica.

This work was supported by the U.S. National Science Foundation through awards AST-0408698 for the ACT project, and PHY-0355328, AST-0707731, and PIRE-0507768. Funding was also provided by Princeton University and the University of Pennsylvania. The PIRE program made possible exchanges between Chile, South Africa, Spain, and the US that enabled this research program. Computations were performed on the GPC supercomputer at the SciNet HPC Consortium. SciNet is funded by: the Canada Foundation for Innovation under the auspices of Compute Canada; the Government of Ontario; Ontario Research Fund-Research Excellence; and the University of Toronto.

T.M. was supported through NASA grant NNX08AH30G. J.B.J. was supported by the FONDECYT grant 3085031. A.D.H. received additional support from a Natural Science and Engineering Research Council of Canada (NSERC) PGS-D scholarship. A.K. and B.P. were partially supported through NSF AST-0546035 and AST-0606975, respectively, for work on ACT. H.Q. and L.I. acknowledge partial support from FONDAP Centro de Astrofísica. N.S. is supported by the U.S. Department of Energy contract to SLAC no. DE-AC3-76SF00515. R.D. was supported by CONICYT, MECESUP, and Fundación Andes. R.H. was supported by the Rhodes Trust. E.S. acknowledges support by NSF Physics Frontier Center grant PHY-0114422 to the Kavli Institute of Cosmological Physics. Y.T.L. acknowledges support from the World Premier International Research Center Initiative, MEXT, Japan. The ACT data will be made public through LAMBDA (<http://lambda.gsfc.nasa.gov/>) and the ACT Web site (<http://www.physics.princeton.edu/act/>).

APPENDIX

The catalog of 157 ACT extragalactic sources is given in Table A1.

REFERENCES

- Austermann, J. E., et al. 2010, *MNRAS*, **401**, 160
 Battaglia, N., Bond, J. R., Frommer, C., Sievers, J. L., & Sijacki, D. 2010, *ApJ*, **725**, 91
 Becker, R. H., White, R. L., & Helfand, D. J. 1995, *ApJ*, **450**, 559
 Best, P. N., von der Linden, A., Kauffmann, G., Heckman, T. M., & Kaiser, C. R. 2007, *MNRAS*, **379**, 894
 Böhringer, H., et al. 2004, *A&A*, **425**, 367
 Cleary, K. A., et al. 2006, VizieR Online Data Catalog, 736, 340
 Condon, J. J., Cotton, W. D., Greisen, E. W., Yin, Q. F., Perley, R. A., Taylor, G. B., & Broderick, J. J. 1998, *AJ*, **115**, 1693
 Coppin, K., Halpern, M., Scott, D., Borys, C., & Chapman, S. 2005, *MNRAS*, **357**, 1022
 Crawford, T. M., Switzer, E. R., Holzapfel, W. L., Reichardt, C. L., Marrone, D. P., & Vieira, J. D. 2010, *ApJ*, **718**, 513
 de Zotti, G., Massardi, M., Negrello, M., & Wall, J. 2010, *A&AR*, **18**, 1
 De Zotti, G., Ricci, R., Mesa, D., Silva, L., Mazzotta, P., Toffolatti, L., & González-Nuevo, J. 2005, *A&A*, **431**, 893
 Fowler, J. W., et al. 2010, *ApJ*, **722**, 1148
 Hall, N. R., et al. 2010, *ApJ*, **718**, 632
 Helou, G., & Walker, D. W. (ed.) 1988, *Infrared Astronomical Satellite (IRAS) Catalogs and Atlases. Vol. 7: The Small Scale Structure Catalog* (Washington, DC: GPO)
 Hincks, A. D., et al. 2010, *ApJS*, **191**, 423
 Högbom, J. A. 1974, *A&AS*, **15**, 417
 Kesteven, M. J. L., Bridle, A. H., & Brandie, G. W. 1977, *AJ*, **82**, 541
 Kovac, J. M., Leitch, E. M., Pryke, C., Carlstrom, J. E., Halverson, N. W., & Holzapfel, W. L. 2002, *Nature*, **420**, 772
 Kuo, C. L., et al. 2007, *ApJ*, **664**, 687
 Lagache, G., et al. 2004, *ApJS*, **154**, 112
 Lima, M., Jain, B., Devlin, M., & Aguirre, J. 2010, *ApJ*, **717**, L31
 Lin, Y., & Mohr, J. J. 2007, *ApJS*, **170**, 71
 Lin, Y., Partridge, B., Pober, J. C., Boucheffry, K. E., Burke, S., Klein, J. N., Coish, J. W., & Huppenberger, K. M. 2009, *ApJ*, **694**, 992
 Lueker, M., et al. 2010, *ApJ*, **719**, 1045
 Mason, B. S., et al. 2003, *ApJ*, **591**, 540
 Mauch, T., Murphy, T., Buttery, H. J., Curran, J., Hunstead, R. W., Piestrzynski, B., Robertson, J. G., & Sadler, E. M. 2003, *MNRAS*, **342**, 1117
 Melin, J., Bartlett, J. G., & Delabrouille, J. 2006, *A&A*, **459**, 341
 Menanteau, F., et al. 2010, *ApJ*, **723**, 1523
 Muchovej, S., et al. 2010, *ApJ*, **716**, 521
 Murphy, T., et al. 2010, *MNRAS*, **402**, 2403
 Negrello, M., Perrotta, F., González-Nuevo, J., Silva, L., De Zotti, G., Granato, G. L., Baccigalupi, C., & Danese, L. 2007, *MNRAS*, **377**, 1557
 Nolta, M. R., et al. 2009, *ApJS*, **180**, 296
 Press, W. H., Teukolsky, S. A., Vetterling, W. T., & Flannery, B. P. 1992, *Numerical Recipes in C: The Art of Scientific Computing* (2nd ed.; Cambridge: Cambridge Univ. Press)
 Reichardt, C. L., et al. 2009, *ApJ*, **701**, 1958
 Scott, K. S., et al. 2008, *MNRAS*, **385**, 2225
 Sehgal, N., et al. 2010, *ApJ*, **709**, 920
 Shaw, L. D., Nagai, D., Bhattacharya, S., & Lau, E. T. 2010, *ApJ*, **725**, 1452
 Staniszewski, Z., et al. 2009, *ApJ*, **701**, 32
 Sunyaev, R. A., & Zel'dovich, Y. B. 1970, *Comments Astrophys. Space Phys.*, **2**, 66
 Swetz, D. S., et al. 2010, arXiv:1007.0290
 Tegmark, M., & de Oliveira-Costa, A. 1998, *ApJ*, **500**, L83
 Toffolatti, L., Argüeso Gomez, F., De Zotti, G., Mazzei, P., Franceschini, A., Danese, L., & Burigana, C. 1998, *MNRAS*, **297**, 117
 Trac, H., Bode, P., & Ostriker, J. P. 2011, *ApJ*, **727**, 94
 Valtaoja, E., Terasranta, H., Urpo, S., Nesterov, N. S., Lainela, M., & Valtonen, M. 1992, *A&A*, **254**, 80
 Vanderlinde, K., et al. 2010, *ApJ*, **722**, 1180
 Vieira, J. D., et al. 2010, *ApJ*, **719**, 763
 Weiland, J. L., et al. 2011, *ApJS*, **192**, 19
 Wright, E. L., et al. 2009, *ApJS*, **180**, 283